The Autophagy Receptor NBR1 Directs the Clearance of Photodamaged Chloroplasts

Han Nim Lee[1,2], Jenu Varghese Chacko[1], Ariadna Gonzalez Solís[1,2], Kuo-En Chen[3], Jessica Barros[3], Santiago Signorelli[4,5], A. Harvey Millar[4], Richard D. Vierstra[3], Kevin W. Eliceiri[1,6,7,8], and Marisa S. Otegui[1,2,*]

[1] Center for Quantitative Cell Imaging, University of Wisconsin-Madison, Madison, Wisconsin, USA.
[2] Department of Botany, University of Wisconsin-Madison, Madison, Wisconsin, USA.
[3] Department of Biology, Washington University in St. Louis, St. Louis, Missouri, USA.
[4] ARC Centre of Excellence in Plant Energy Biology, School of Molecular Sciences, The University of Western Australia, Perth, West Australia, Australia.
[5] Department of Plant Biology, School of Agronomy, Universidad de la República, Montevideo Uruguay.
[5] Department of Medical Physics, University of Wisconsin-Madison, Madison, Wisconsin, USA.
[7] Department of Biomedical Engineering, University of Wisconsin-Madison, Madison, Wisconsin, USA
[8] Morgridge Institute for Research, Madison, Wisconsin, USA.

* Corresponding author: Marisa S. Otegui; otegui@wisc.edu

Abstract

The ubiquitin-binding NBR1 autophagy receptor plays a prominent role in recognizing ubiquitylated protein aggregates for vacuolar degradation by macroautophagy. Here, we show that upon exposing Arabidopsis plants to intense light, NBR1 associates with photodamaged chloroplasts independently of ATG7, a core component of the canonical autophagy machinery. NBR1 coats both the surface and interior of chloroplasts, which is then followed by direct engulfment of the organelles into the central vacuole via a microautophagy-type process. The relocalization of NBR1 into chloroplasts does not require the chloroplast translocon complexes embedded in the envelope but is instead greatly enhanced by removing the self-oligomerization mPB1 domain of NBR1. The delivery of NBR1-decorated chloroplasts into vacuoles depends on the ubiquitin-binding UBA2 domain of NBR1 but is independent of the ubiquitin E3 ligases SP1 and PUB4, known to direct the ubiquitylation of chloroplast surface proteins. Compared to wild-type plants, *nbr1* mutants have altered levels of a subset of chloroplast proteins and display abnormal chloroplast density and sizes upon high light exposure. We postulate that, as photodamaged chloroplasts lose envelope integrity, cytosolic ligases reach the chloroplast interior to ubiquitylate thylakoid and stroma proteins which are then recognized by NBR1 for autophagic clearance. This study uncovers a new function of NBR1 in the degradation of damaged chloroplasts by microautophagy.

Keywords: NBR1, chlorophagy, microautophagy, ubiquitin.

Introduction

Autophagy is a process by which cytoplasmic contents including organelles, individual proteins, protein complexes and cytosolic aggregates, collectively called autophagic cargo, are delivered to vacuoles (plants and yeast) and lysosomes (animals) for degradation (Mizushima et al., 1998). In plants, autophagy most commonly occurs through the formation of cargo-sequestering double-membrane-bound organelles called autophagosomes (macroautophagy) or through the direct engulfment of cargo by the vacuolar membrane (microautophagy). Whereas the molecular underpinnings of microautophagy are poorly understood, the machinery for macroautophagy involves more than 40 ATG (Autophagy Related) proteins whose actions are regulated by upstream phosphorylation events ultimately leading to formation of autophagosomes decorated with a conjugate of ATG8 with phosphatidylethanolamine (PE) (Xie et al., 2008). This conjugation is mediated an enzymatic cascade sequentially involving the activating enzyme ATG7, the conjugating enzyme ATG3, and a ligase complex comprising an ATG5-ATG12 conjugate complexed with ATG16 (Ohsumi, 2001). The resulting ATG8-PE adduct is not only required for autophagosomes assembly but also, through its interaction with a host of autophagic receptors, for the selection of appropriate autophagic cargo (Noda et al., 2008).

There are several selective autophagy receptors that specifically recognize ubiquitylated cargo. Among them, metazoan SQSTM1/p62 (Sequestosome 1) and NBR1 (NEIGHBOR OF BRCA1 gene 1) promote the accretion of ubiquitylated proteins into larger condensates which are then encapsulated by autophagosomes for macroautophagic clearance (aggrephagy) (Bjørkøy et al., 2005; Komatsu et al., 2007; Nezis et al., 2008; Turco et al., 2021; Rasmussen et al., 2022). The PB1 (Phox and Bem1 domain) domain present in both SQTM1 and NBR1 mediate their mutual interaction and oligomerization into helical filaments (Ciuffa et al., 2015) which then promote the aggregation of ubiquitylated species (Jakobi et al., 2020; Turco et al., 2021). In addition, mammalian SQSTM1 and NBR1 share a zinc-finger domain (ZZ) that can bind N-terminally arginylated proteins, lysine-48 (K48)- and K63-linked polyubiquitylated proteins, and other cargo (Cha-Molstad et al., 2015; Kwon et al., 2018; Wang et al., 2021), a ubiquitin-associated (UBA) domain with affinity for ubiquitin, and an ATG8-interacting motif (AIM) sequence that binds ATG8 (Seibenhener et al., 2004; Ichimura et al., 2008; Zientara-Rytter et al., 2011; Sun et al., 2022a). NBR1, but not SQSTM1, also contains a Four-Tryptophan (FW) domain, which at least in some fungal species recognizes cargo for selective autophagy. The plant NBR1 proteins uniquely harbor two UBA domains but only the C-terminal

sequence (UBA2) binds ubiquitin (Svenning et al., 2011). Through these collective features, SQSTM1 and NBR1 can mediate selective autophagy of cargo in both ubiquitin and ubiquitin-independent manners. Most non-metazoan species encode only NBR1, whereas metazoans can express either or both SQTM1 and NBR1 (Svenning et al., 2011).

In plants, NBR1 has been connected genetically to numerous physiological processes (Zhang and Chen, 2020). For example, it modulates tolerance to heat stress through at least two mechanisms; recognition and sorting for degradation of proteotoxic ubiquitylated aggregates that accumulate at high temperatures (Zhou et al., 2013; Zhou et al., 2014), and the negative regulation of heat stress memory by mediating the clearance of heat-shock-related chaperones and their co-factors (Thirumalaikumar et al., 2021). Arabidopsis NBR1 also targets for autophagic clearance: (i) the exocyst subunit EXO70E2 and its associated organelle EXPO (Ji et al., 2020), (ii) misfolded protein aggregates (Jung et al., 2020), and (iii) viral capsid proteins (Hafren et al., 2017) and pathogenic bacterial effectors (Dagdas et al., 2016; Dagdas et al., 2018; Üstün et al., 2018; Leong et al., 2022). Remarkably, Arabidopsis null *nbr1* mutants develop normally under favorable growth conditions and are still able to execute general autophagy (Jung et al., 2020) and the selective clearance of certain organelles such as peroxisomes (Young et al., 2019). However, the mutants are hypersensitive to heat, drought, oxidative, and salt stress and over-accumulate cytoplasmic protein aggregates (Zhou et al., 2013). Taken together, NBR1 appears to be required for some but not all autophagy-dependent events, consistent with a role in selective autophagy.

Chloroplast turnover involves multiple routes that are dependent on autophagy and/or the ubiquitin-proteasome system. Several ATG8-dependent autophagic routes control the piecemeal turnover of chloroplast components *via* Rubisco-containing bodies (Chiba et al., 2003; Ishida et al., 2008; Spitzer et al., 2015), ATI1-PS (ATG8-INTERACTING PROTEIN 1) bodies (Michaeli et al., 2014), and SSLG (small starch-like granule) bodies (Wang et al., 2013) as well as the engulfment of whole photodamaged chloroplasts through microautophagy (Izumi et al., 2017). Outer envelope proteins, including components of the outer envelope translocon complex (TOC), can be ubiquitylated by chloroplast membrane-localized ubiquitin E3 ligase SP1 (SUPPRESOR OF PPI1 LOCUS 1) and extracted from the envelope membrane by the β-barrel channel protein SP2 and the AAA+ ATPase CDC48 for degradation by the 26S proteasome in a process named chloroplast-associated degradation (CHLORAD) (Ling et al., 2012; Ling et al., 2019). The cytosolic E3 ligase PLANT U-BOX4 (PUB4) also ubiquitylates chloroplast envelope proteins in response to oxidative stress (Woodson et al., 2015). More recently, proteins within

the chloroplast lumen (*e.g.* thylakoid and stroma proteins) were also shown to be targeted by ubiquitylation for break down *via* the proteasomes under oxidative stress (Li et al., 2022; Sun et al., 2022b). However, it remains unclear how ubiquitylation occurs inside chloroplasts.

Here, we show that NBR1 associates with photodamaged chloroplasts *via* its ubiquitin-binding UBA domain and mediates their vacuolar degradation by an autophagic pathway independent of ATG7, and therefore, of ATG8 lipidation. NBR1 associates with the surface and interior of chloroplasts without the need for intact translocon complexes within the outer and inner membranes. We proposed that photodamaged chloroplasts lose structural integrity of their envelopes, thus allowing access of cytosolic components such as the ubiquitylation machinery and NBR1 into the plastid interior and microautophagic clearance.

Results

NBR1 associate with chloroplasts upon exposure to high light.

To determine whether the autophagy receptor NBR1 is involved in chloroplast turnover upon photoradiation damage, we imaged by confocal microscopy the NBR1-GFP fusion protein expressed under the control of the NBR1 promoter (*ProNBR1:NBR1-GFP*; (Hafren et al., 2017; Thirumalaikumar et al., 2021) in seedlings grown under low light (LL; 40 µmol m^{-2} s^{-1}) at 22ºC and exposed to high light (HL; 1500 µmol m^{-2} s^{-1}) at 12ºC for 2 h, with a focus on the sub-adaxial epidermal mesophyll layer (mesophyll cells under the cotyledon adaxial epidermis) exposed to HL. Under LL, NBR1 was typically found in cytosolic puncta within cotyledons that likely represent aggresome condensates (Svenning et al., 2011; Jung et al., 2020) and did not colocalize with chloroplasts seen by chlorophyll autofluorescence (Fig. 1). After exposing seedlings to HL and allowing them to recover under LL for 24 h, 2% of the chloroplasts in HL-exposed mesophyll cells became heavily decorated with NBR1-GFP (Fig. 1A, B). NBR1-GFP either coated the surface of these chloroplasts or, in a few cases, localized inside (Fig. 1A). Some NBR1-GFP signal in hypocotyl cells was also associated with stromules (Fig. 1A).

To determine whether NBR1-GFP associated with photodamaged chloroplasts, we measured chlorophyll intrinsic fluorescence from seedlings either kept under LL or left to recover after HL exposure. In cotyledons exposed to HL, chloroplasts not labeled by NBR1-GFP had chlorophyll intensity values similar to those of control chloroplasts kept under LL. In contrast, NBR1-GFP-decorated chloroplasts showed a significant decrease in chlorophyll fluorescence intensity (Fig. 1C), consistent with chlorophyll breakdown after photodamage (Nakamura et al., 2018). As an indicator of chloroplast photodamage, we quantified the

chlorophyll fluorescence intensity ratio measured at 517 and 683 nm (Nakamura et al., 2018), and found a statistically significant increase in this ratio for NBR1-GFP-decorated chloroplasts after HL exposure (Fig. 1D).

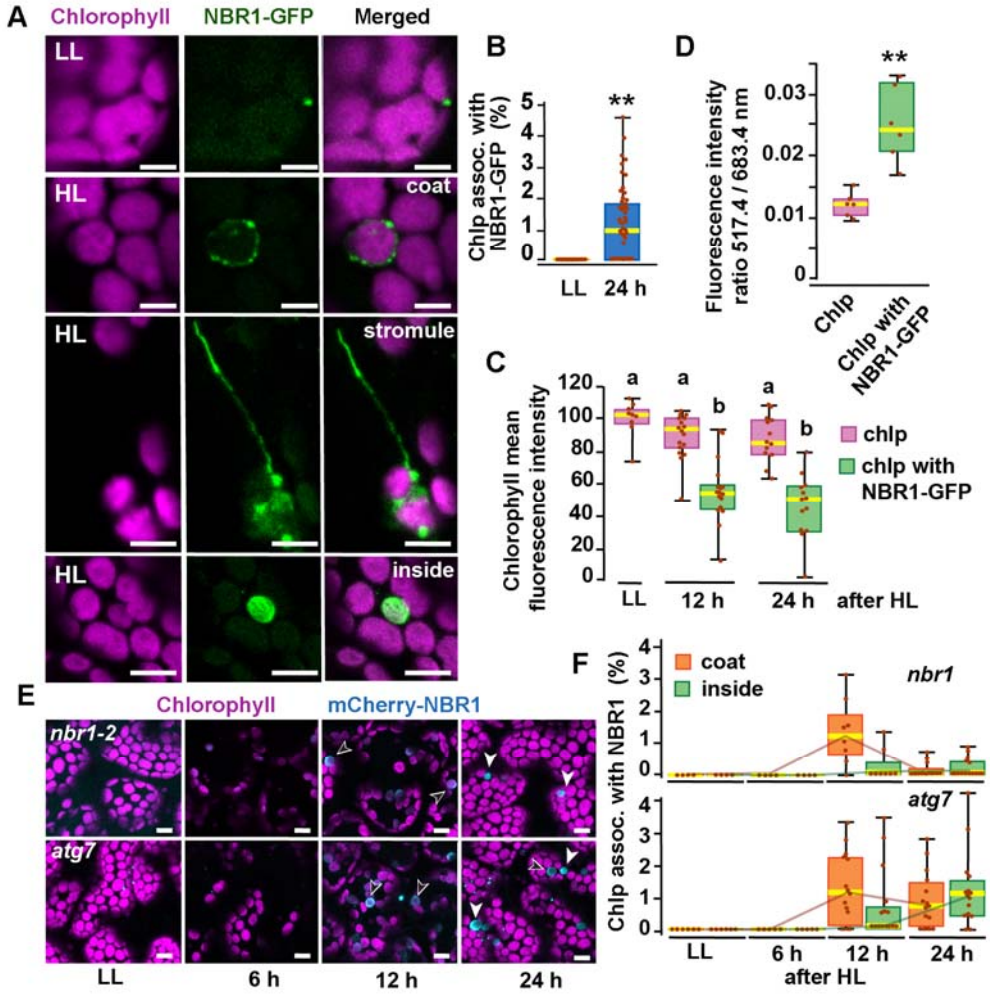

Figure 1. NBR1 associates with chloroplasts after HL exposure.

(A) Confocal imaging of NBR1-GFP and chlorophyll autofluorescence in cotyledons and hypocotyl cells of 8-day old wild type seedlings grown under low light (LL, 40 µmol m^{-2} s^{-1}) or left to recover for 24 h after exposure to 2 h HL conditions (HL, 1,500 µmol m^{-2} s^{-1}) at 12°C. After HL exposure, NBR1 either coated the surface of chloroplasts and stromules or localized inside chloroplasts.

(B) Box and whisker plots represent the percentage of chloroplast associated with NBR1-GFP in 8-day old seedlings grown under LL or 24 h after HL exposure. At least 35 confocal images from 7-12 cotyledons were analyzed for each condition.

(C) Box and whisker plots showing chlorophyll mean intensity from chloroplast with and without NBR1-GFP in cotyledons from 8-day old seedling grown under LL or exposed to HL and left to recover for 12 h

or 24 h. Representative experiment showing data from at least 5 randomly selected chloroplasts for each condition.

(D) Ratio of chlorophyll fluorescence intensities at 517.4 m and 683.4 nm. Representative experiment showing data from 6 chloroplasts with or without NBR1-GFP from 8-day old cotyledons 24 h after HL exposure. Different letters on the graph indicate significant difference ($p < 0.05$) calculated by one-way ANOVA followed by Tukey's test.

(E) Confocal imaging of cotyledons from 8-day old seedling expressing mCherry-NBR1 in *nbr1* and *atg7* plants grown under LL or exposed to HL and left to recover for 6, 12, and 24 h. Hollow arrowheads and filled arrowheads indicate the mCherry-NBR1 coats and inside chloroplasts, respectively.

(F) Box and whisker plots showing the percentage of chloroplasts associated with mCherry-NBR1 as coats (orange) or inside chloroplasts (green) under LL, and at the indicated recovery times after HL exposure. The top and bottom plots show measurements from *nbr1* and *atg7,* respectively. Representative experiment analyzing between 4 and 15 fields from 3-6 cotyledons for each condition and genotype.

Box and whisker plots in B, C, D, and F display the variation in data through quartiles; the middle line indicates the median and whiskers show the upper and lower fences. Asterisks in B and D denote significant differences based on t-tests (**, $p < 0.01$).

Scale bars = 5 μm in A and E.

Previous studies showed that the recruitment of ATG8 to chloroplasts after HL exposure depends on the canonical ATG machinery (Nakamura et al., 2018). Consequently, we tested whether this was also the case for NBR1 by analyzing seedlings expressing mCherry-NBR1 under the control of the *UB10* promoter in the *nbr1-2* (*nbr1*; Zhou et al., 2013; Jung et al., 2020) and *atg7-2* (*atg7*; Chung et al., 2010) mutant backgrounds. Upon HL exposure, we detected by confocal microscopy mCherry-NBR1 associated with chloroplasts in both *nbr1* and *atg7* cotyledon mesophyll cells (Fig. 1E, F). In both genotypes, the mCherry-NBR1 signal coated the chloroplast surface (open arrows in Fig. 1E) as well as its interior (solid arrows in Fig. 1E), indicating that ATG7, and by inference ATG8 lipidation, are not required for recruiting NBR1 to chloroplasts upon HL exposure.

To confirm that NBR1 was indeed internalized into chloroplasts, we examined the ultrastructural features of chloroplasts under HL conditions by transmission electron microscopy and localized NBR1 with anti-NBR1 antibodies. First, we analyzed the structural alterations of chloroplasts after 24 h exposure to HL in wild-type, *atg7*, and *nbr1* cotyledons processed by high-pressure frozen/freeze substitution. Based on the degree of structural integrity, we found three morphologically distinct chloroplast types often in the same cell although with different

frequencies. Type-1 chloroplasts had normal thylakoids and electron-dense stroma; Type-2 chloroplasts had dilated and lighter stroma with thylakoid membranes partially disorganized and displaced to one side of the chloroplast; and Type-3 chloroplasts contained highly disorganized thylakoids, light stroma, and clear signs of chloroplast envelope rupture (Fig. 2A-C).

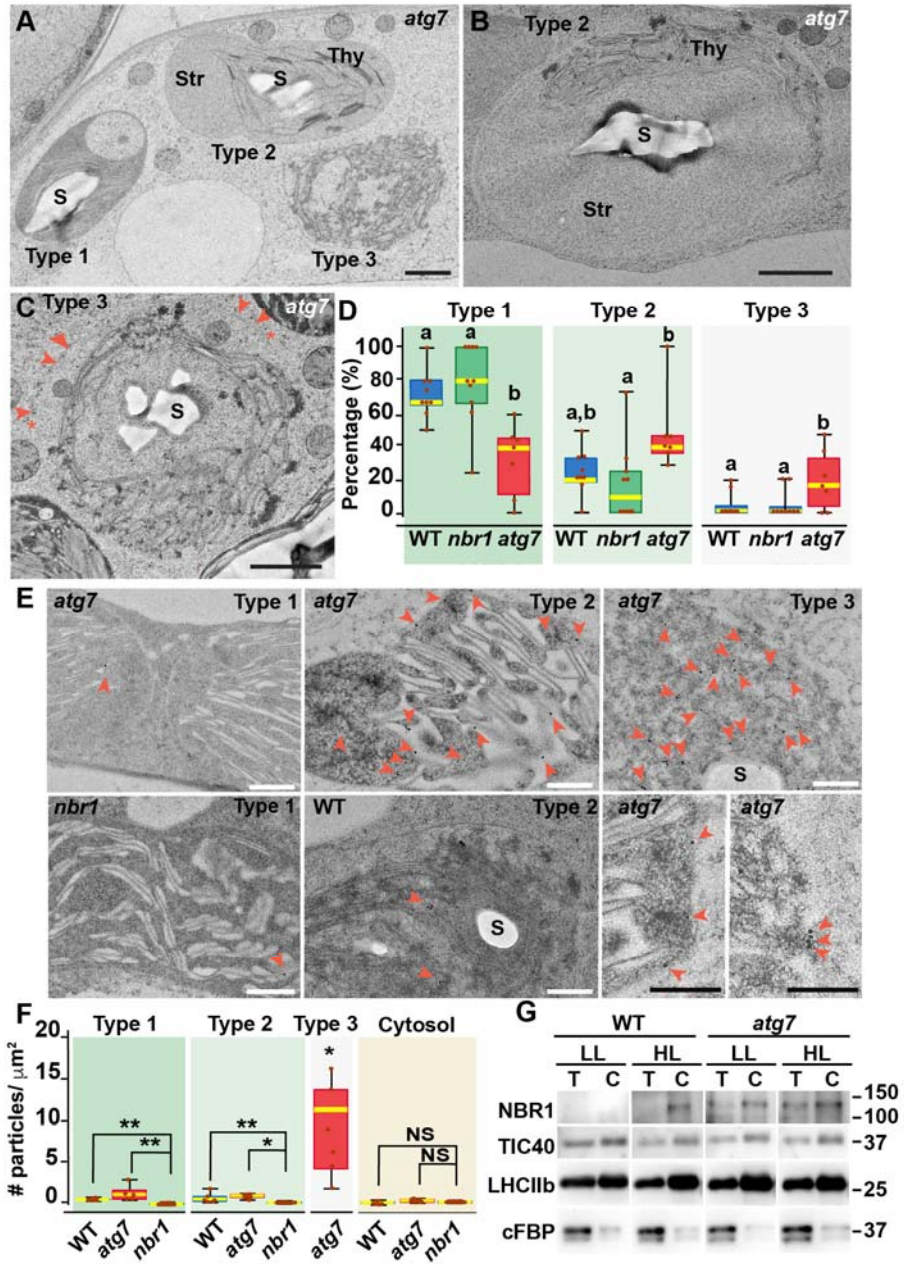

Figure 2. Ultrastructure of chloroplasts in wild-type, *atg7*, and *nbr1* cotyledons 24 h after HL exposure.

(A) Transmission electron micrograph of a high-pressure frozen/freeze-substituted *atg7* cotyledon mesophyll cell from 8-day old seedlings exposed to HL and left to recover for 24 h. Three different types

of chloroplasts based on their structural integrity are seen. Type-1 chloroplasts with electron dense stroma and tightly appressed thylakoids, Type-2 chloroplasts with lighter stroma and partially disorganized thylakoids, and Type-3 chloroplasts with ruptured envelopes, disorganized thylakoid membranes and a stroma region with similar electron density and appearance to the cytoplasm.
(B, C) Representative Type-2 **(B)** and Type-3 **(C)** chloroplasts in an *atg7* mesophyll cells. Note in (C) that the outer and inner envelopes (arrowheads) are disrupted in several sites (asterisks) exposing the interior of the chloroplast, including thylakoid membranes to the cytosol.
(D) Box and whisker plots showing the percentage of Type-1, -2, and -3 chloroplasts per mesophyll cell section in wild-type Col-0 (WT), *nbr1*, and *atg7* cotyledons. Different letters on the graph indicate significant difference ($p < 0.05$) calculated by one-way ANOVA followed by Tukey's test.
(E) Immunogold labeling with anti NBR1 antibodies on chloroplasts of WT, *nbr1*, and *atg7* mutant mesophyll cells exposed to HL followed by 24 h recovery. Red arrowheads indicate gold particles on chloroplasts.
(F) Quantification of anti-NBR1 gold labeling on Type-1, -2, and -3 chloroplasts and cytoplasm from WT, *atg7*, and *nbr1* mutant mesophyll cells exposed to HL. A t-test was used to compare values between mutant and WT samples; * and ** indicate $p < 0.05$ and $p < 0.01$, respectively.
(G) Immunoblot detection of NBR1, TIC40 (chloroplast inner envelope protein), LHCIIb (thylakoid protein), and cFBP (cytosolic protein) in total protein extracts (T) and chloroplast protein fraction (C) from 4-week-old WT and *atg7* plants grown under LL or exposed to HL and let recover for 24h.
Box and whisker plots in D and F show the variation in data through quartiles; the middle line indicates the median and whiskers show the upper and lower fences.
S, starch; St, stroma; Thy, thylakoids. Scale bars: 1 μm in A, B, C; 500 nm in E.

Type-3 chloroplasts were significantly more abundant in the *atg7* cotyledons, whereas their frequency in *nbr1* cotyledons was indistinguishable from that in wild-type cotyledons (Fig. 2D). Using anti-NBR1 antibodies (Figure 2-figure supplement 1), we performed immunogold labeling to detect the native NBR1 protein in the three types of chloroplasts from wild-type and *atg7* cotyledons exposed to HL, in this case using *nbr1* seedlings grown under similar conditions as a negative control (Fig. 2E, F). Whereas we did not detect labeling of NBR1 in the cytosol, all chloroplasts in wild-type and *atg7* seedlings exposed to HL showed significantly higher labeling than those seen in the *nbr1* cotyledons (Fig. 2E, F).

Corroborating the NBR1-GFP and mCherry-NBR1 confocal imaging results, endogenous NBR1 was detected on the surface and inside wild-type and *atg7* chloroplasts (Fig. 2E). Among the three types of chloroplasts, Type-3 chloroplasts, which were most abundant in *atg7* cotyledons (Fig. 2D), showed the heaviest internal labeling, both on thylakoids and on the

stroma (Fig. 2F). As Type-3 chloroplasts showed disorganized thylakoids, this labeling is consistent with the preferential recruitment of NBR1-GFP to damaged chloroplasts as judged by their decreased levels of chlorophyll autofluorescence (Fig. 1C).

To further corroborate the association of NBR1 with photodamaged chloroplasts, we isolated chloroplasts from 4-week-old wild-type and *atg7* mutant plants kept under LL or exposed to HL conditions and allowed to recover for 24 h (Fig. 2G). We assessed the purity of our chloroplast fraction by testing the enrichment of chloroplast proteins such as TIC40 (inner envelope) and anti-LHCIIb (thylakoid), and the depletion of the cytosolic fructose bisphosphatase (FBPase). NBR1 was barely detectable in either the total extract or the chloroplast fraction from wild-type plants kept under LL (Fig. 2G). However, after HL exposure, NBR1 became much more abundant in the chloroplast fraction. Similarly, the association of NBR1 with chloroplasts under HL was also apparent in *atg7* seedlings (Fig. 2G), further confirming that ATG7 is not required for recruiting NBR1 to photodamaged chloroplasts.

ATG8 and NBR1 are recruited to different populations of damaged chloroplasts.

ATG8 was previously reported to coat photodamaged chloroplasts in *Arabidopsis* (Nakamura et al., 2018). Since NBR1 interacts with ATG8, we tested whether NBR1 and ATG8 were recruited to the same chloroplast population. We used seedlings expressing both mCherry-NBR1 and GFP-ATG8, exposed them to HL, and then imaged them during a 24 h recovery window (Fig. 3A, B). As expected, neither mCherry-NBR1 or GFP-ATG8 associated with chloroplasts under LL conditions. However, after the HL treatment, the chloroplast association of both proteins became evident at 6 h during recovery. By 12 h after HL exposure, approximately 4% and 5% of the total mesophyll chloroplasts were decorated by either mCherry-NBR1 or GFP-ATG8, respectively, but only 1% of chloroplasts were decorated with both (Fig. 3A, B). A similar trend was observed 24 h after HL exposure; approximately 7% of the chloroplasts were labeled with GFP-ATG8, 5.5% were labeled with mCherry-NBR1 but only 2% of the chloroplasts were associated with both (Fig 3A, B). This dichotomy suggests that NBR1 and ATG8 are recruited to unique populations of chloroplasts, consistent with their distinct dependence on the ATG machinery for chloroplast recruitment.

To further assess a functional disconnection between ATG8 and NBR1 in the degradation of photodamaged chloroplasts, we imaged GFP-ATG8A in *nbr1*, *atg7*, and wild-type seedlings exposed to HL (Fig. 3C, D). As previously reported (Nakamura et al., 2018),

GFP-ATG8 failed to label photodamaged chloroplasts in *atg7* cotyledons. Compared to wild type, we detected a significant decrease in the proportion of chloroplasts decorated by GFP-ATG8A in the *nbr1* mutant at 6 h during recovery from HL exposure; however, by 24 h, similar proportions of both wild type and *nbr1* chloroplasts were coated by GFP-ATG8A (Fig. 3C, D). Taken together, these results show that NBR1 and ATG8A are recruited to different populations of photodamaged chloroplasts and that NBR1 is only partially required for the early association of GFP-ATG8A with these organelles.

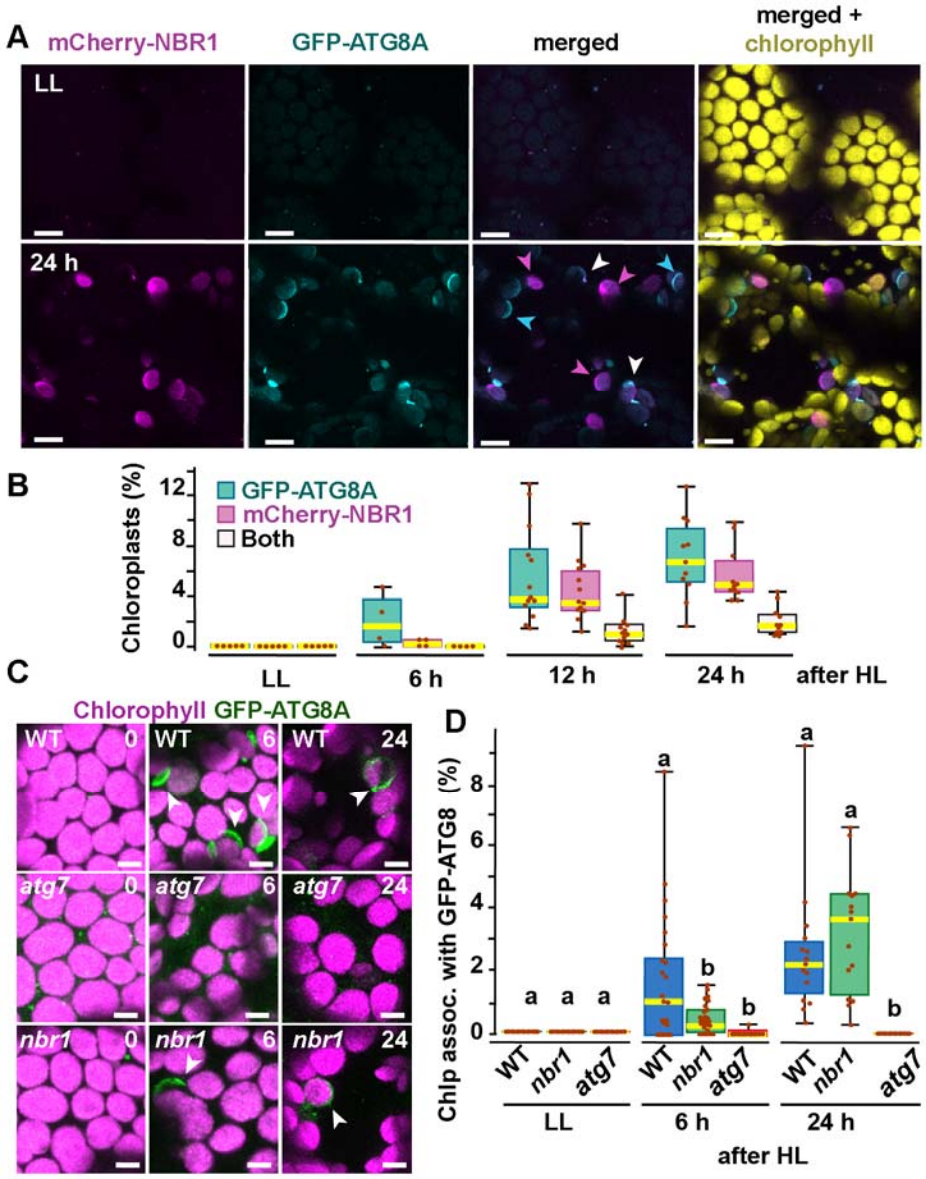

Figure 3. Recruitment of NBR1 and ATG8A to photodamaged chloroplasts.

(A) Confocal imaging of cotyledon mesophyll cells from 8-day old seedlings expressing mCherry-NBR1 and GFP-ATG8A under LL (top) and at 24 h after HL exposure (bottom). Magenta, cyan, and white arrowheads indicate chloroplasts associated with mCherry-NBR1, GFP-ATG8, or both, respectively.
(B) Box and whisker plots showing the percentage of chloroplasts associated with GFP-ATG8A (cyan), mCherry-NBR1 (magenta), or both (white) under LL and during recovery after HL exposure.
(C) Confocal imaging of GFP-ATG8A in cotyledons of 8-day old wild-type Col-0 (WT), *atg7*, and *nbr1* seedlings grown under LL, and 6 and 24 h after HL treatment. Arrowheads indicate chloroplasts associated with GFP-ATG8A.
(D) Box and whisker plot displaying the percentage of chloroplast associated with GFP-ATG8A in different genotypes, under LL and recovery after HL. Different letters on the graph indicate significant difference ($P < 0.05$) calculated by one-way ANOVA followed by Tukey's test.
Box and whisker plots in B and D show the variation in data through quartiles; the middle line indicates the median and whiskers show the upper and lower fences.
Scale bars: 10 µm in A and C.

NBR1-decorated chloroplasts are delivered to vacuoles in an ATG7-independent manner.

Previous studies have shown that ATG8-associated chloroplasts are delivered to vacuoles through a microautophagic process that relies on the canonical ATG machinery (Izumi et al., 2017; Nakamura et al., 2018). To determine whether this is also the case for NBR1-decorated chloroplasts, we co-expressed mCherry-NBR1 with the tonoplast marker YFP-VAMP711 (Geldner et al., 2009) in *nbr1* seedlings. After HL exposure, mCherry-NBR1-positive chloroplasts associated with deep tonoplast invaginations (Fig. 4A), which led to their vacuolar internalization by microautophagy, in a process topologically similar to that previously described for ATG8-decorated chloroplasts (Izumi et al., 2017). Similarly, we were able to detect NBR1-positive chloroplasts inside vacuoles of the mCherry-NBR1 seedlings stained with the vacuolar dye BCECF (Scheuring et al., 2015) 24 h after HL exposure (Fig. 4B, C). Surprisingly, NBR1-decorated chloroplasts were also seen inside vacuoles of *atg7* seedlings (Fig. 4B, C).

Taken together, these results are consistent with NBR1 associating with chloroplasts targeted for vacuolar degradation through ATG7-independent microautophagy. In addition, the higher number of NBR1-positive photodamaged chloroplasts in *atg7* seedlings (Fig. 2) does not seem to arise from a failure to deliver these chloroplasts to the vacuole but more likely to the higher accumulation of photodamaged chloroplasts in the *atg7* mutant.

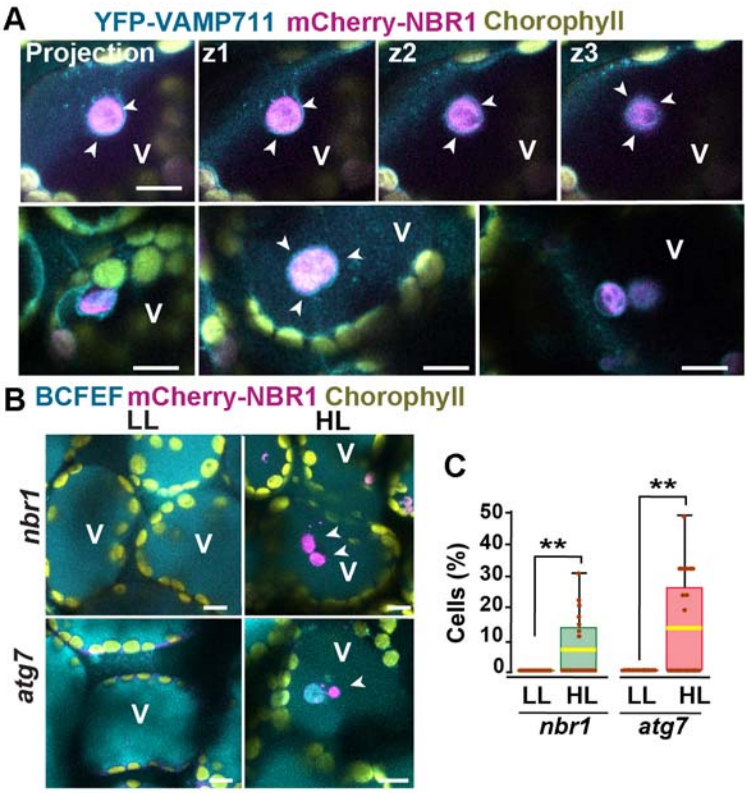

Figure 4: Vacuolar delivery of NBR1-positive chloroplast into the vacuole.

(A) Projection of three confocal images (z1-z3) and several other confocal images of cotyledon mesophyll cells from1-week-old, wild-type seedlings expressing the tonoplast marker YFP-VAMP711 and mCherry-NBR1, 24 h after HL exposure. Chloroplast labeled by mCherry-NBR1 were surrounded by the tonoplast (arrowheads) and internalized into the vacuole (V) through microautophagy.

(B) Confocal images of *nbr1* and *atg7* cotyledon mesophyll cells at 24 h after HL exposure and stained with the vacuolar dye BCECF. Note the mCherry-NBR1-labeled chloroplasts inside the vacuoles.

(C) Box and whisker plot displaying the percentage of cells containing mCherry-NBR1-labeled chloroplasts inside their vacuoles. Boxes show the variation in data through quartiles; the middle line indicates the median and whiskers show the upper and lower fences.

A t-test was used to compare values between LL and recovery after HL ** indicate $p < 0.01$.

Scale bars: 10 µm in A and B.

Impaired remodeling of chloroplasts in *atg7* and *nbr1* mutants.

If NBR1 is critical for targeting photodamaged chloroplasts to the vacuole, we reasoned that *nbr1* mutations would reduce the loss of chloroplasts after HL, as it has been shown for the *atg5* and *atg7* mutants (Izumi et al., 2017). To test this scenario, we expressed RECA-GFP, a

stromal marker bearing the transit peptide of Arabidopsis RECA fused to GFP (Kohler et al., 1997; Spitzer et al., 2015), and imaged the cotyledon sub-adaxial epidermal mesophyll layer from 8-day-old seedlings by confocal microscopy. We found that, under LL conditions *atg7* but not *nbr1* mutant seedlings had a higher density of chloroplasts compared to wild type (Fig. 5A, B). Twenty four hours after HL, there was a reduction in chloroplast density in all three genotypes but the decrease was less pronounced in *atg7* and *nbr1* (17% and 16% reduction, respectively) compared to the wild-type control (25% reduction; Fig. 5A, B), consistent with impaired turnover of chloroplasts in both *atg7* and *nbr1* mutants.

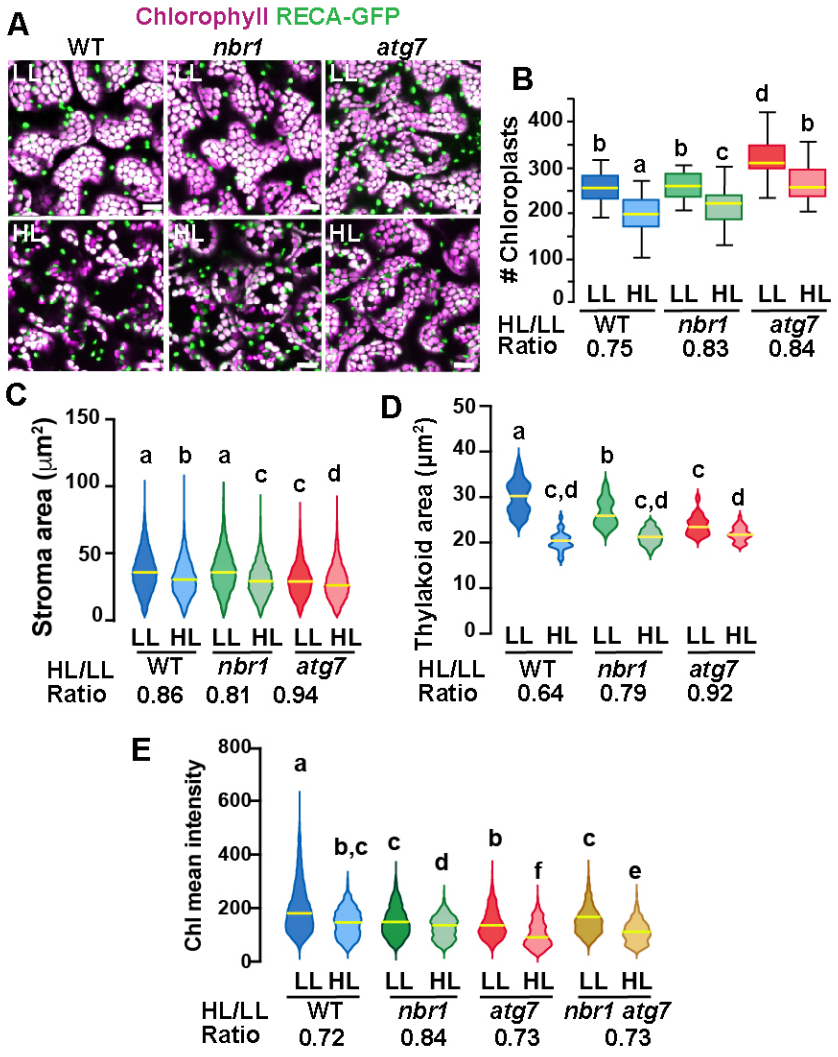

Figure 5. Chloroplast remodeling after HL exposure.

(A) Projections of 20 confocal images along a z-stack taken from the adaxial side of cotyledon mesophyll cells from 8-day old wild-type (WT), *atg7*, and *nbr1* seedlings expressing RECA-GFP. Seedlings were grown under LL, exposed to HL for 2 h and let recover for 24 h.

(B) Chloroplast density in adaxial-facing mesophyll cells (number of chloroplasts per 2.16 μm^2) based on confocal images. At least 20 randomly selected areas from 6-9 cotyledons were considered in this analysis. Boxes show the variation in data through quartiles; the middle line indicates the median and whiskers show the upper and lower fences.
(C) Stroma area (μm^2) as measured by the RECA-GFP fluorescence signal per individual chloroplast imaged by confocal microscopy. Lines in violin plots indicate median values. At least 25 individual chloroplasts were measured for each genotype and condition.
(D) Thylakoid area (μm^2) as measured by chlorophyll fluorescence signal area per individual chloroplast. Line in violin plots indicate median values. At least 5,000 individual chloroplasts were measured for each genotype and condition.
(E) Chlorophyll mean intensities measured in individual chloroplasts by multiphoton imaging. Between 1,300 and 2,600 individual chloroplasts were measured for each genotype and condition. Lines in violin plot indicate median values.
In B to E, the HL/LL ratio was calculated by dividing the average value from HL-treated plants by the average value of the plants grown under LL. Different letters denote significant differences from each other based on two-way ANOVA followed by Tukey's test ($p < 0.05$).
Scale bars: 10 μm in A.

To examine whether chloroplast size also changed upon HL exposure, we measured the area of both RECA-GFP signal (stroma) and chlorophyll autofluorescence (thylakoids) in individual chloroplasts. Overall, there was a decrease in both RECA-GFP and chlorophyll area of individual chloroplasts 24 h after HL exposure in the three genotypes. However, whereas the *nbr1* and wild type RECA-GFP-decorated chloroplasts were similar in size under LL, the decrease in RECA-GFP area upon HL treatment was slightly more abrupt in *nbr1* (19% reduction) than in control cotyledons (14% reduction; Fig. 5A, C). RECA-GFP-decorated *atg7* chloroplasts were smaller than those in control and *nbr1* cotyledons and showed a small (6%) reduction in area upon HL treatment (Fig. 5A, C). Chlorophyll areas were smaller in *nbr1* and *atg7* chloroplasts compared to the wild-type control even under LL conditions, and underwent an attenuated reduction after HL exposure (21% and 18% in *nbr1* and *atg7*, respectively), compared to control chloroplasts (36% reduction; Fig. 5A, D). Taken together, these results demonstrate that although both *atg7* and *nbr1* retained more chloroplasts than control plants after HL exposure (Fig 4E), the remaining chloroplasts in the mutants were smaller, both in stroma and thylakoid areas.

These unique chloroplast dynamics in *nbr1*, *atg7*, and wild-type plants suggested that although ATG7 and NBR1 are both important for chloroplast turnover, they control different

aspects of chloroplast remodeling/turnover after HL radiation. To further understand how chloroplasts are differentially affected, we used multiphoton imaging to excite and measure chlorophyll mean intensities under LL and 24 h after HL exposure in *nbr1* and *atg7* seedlings, together with a previously characterized *nbr1-2 atg7-2* double mutant (*nbr1 atg7*; Jung et al., 2020). Compared to controls, mean chlorophyll fluorescence intensity in all three mutants was weaker than wild type under LL conditions. This intensity decreased approximately 27-28% in wild type and the *atg7* mutant after HL (based on ratio of chlorophyll mean intensities between HL and LL values), but only 16% in the *nbr1* mutant (Fig. 5E). Unexpectedly, the mean chlorophyll intensity values from *nbr1 atg7* mutant under LL and after HL treatment were intermediates between those from the single *nbr1* and *atg7* mutant seedlings. These results indicate that mutations in both *NBR1* and *ATG7* affect either chlorophyll abundance and/or chlorophyll photochemical properties even under LL conditions.

Proteome profiling supports NBR1- and ATG7-dependent pathways for clearing photodamaged chloroplasts.

To further understand the function of NBR1 and ATG7 in chloroplast remodeling and turnover, we analyzed by mass spectrometry (MS) the total proteome of 1-week-old *atg7*, *nbr1*, *nbr1 atg7* double mutant, and wild-type seedlings grown under LL and at 24 h after HL treatment (Fig. 6, Fig. 6-figure supplements 1 and 2, Suppl. Tables 1-3).

HL treatment induced a relatively mild changes in the total proteome of all four genotypes. We identified 164 differentially accumulated proteins (DAPs) after HL treatment as compared to LL (4.5% of the 3682 total detected proteins; 55 more and 109 less abundant) in wild type; 622 DAPs in *atg7* (17% of the 3693 total detected proteins; 444 more and 178 less abundant); 313 DAPs in *nbr1* (8.5% of the 3683 total detected proteins; 166 more and 147 less abundant)*;* and 215 DAPs in the *nbr1 atg7* double mutant (6% of the 3668 total detected proteins; 102 more and 113 less abundant) (Fig. 6-figure supplement 2 and Suppl. Tables 4-7). Compared to wild-type seedlings, the three analyzed mutants showed differences in their proteome profiles under both LL and HL conditions (Fig. 6-figure supplement 2, Suppl. Tables 8-13); under HL and compared to WT, we detected 456 DAPs in *atg7* (166 less and 290 more abundant), 251 DAPs in *nbr1* (170 less and 81 more abundant), and 266 DAP in *nbr1 atg7* (95 less and 171 more abundant) (Fig. 6-figure supplement 2, Suppl. Tables 8-10), showing a general trend of steady-state protein levels increasing in *atg7* and *nbr1 atg7* and decreased protein abundance in *nbr1* mutant seedlings.

In terms of the chloroplast proteome, all genotypes showed changes in protein abundance after HL treatment (Fig. 6A), with an over-representation of less abundant chloroplast proteins in the three mutants as compared to wild type, under both LL and after HL treatment (Fig. 6A, B). This group of less abundant proteins in the three mutants localized to stroma, thylakoids, and envelopes (Fig. 6B). Whereas the proportion of less abundant chloroplast proteins in *atg7* compared to wild type remained constant under LL and HL (4% in both cases), the proportion of less abundant proteins in *nbr1* were 1.8% and 3.3% of the identified chloroplast proteins under LL and HL, respectively. The *nbr1 atg7* mutant showed the opposite trend with fewer less abundant chloroplast proteins after HL (3%) than under LL (5%). Under HL, *atg7* showed a relative increase of approximately 20% in the proportion of less abundant chloroplast proteins compared to the *nbr1* and *nbr1 atg7* mutants (Fig. 6B). Interestingly, only 34-35% of the less abundant chloroplast proteins in *atg7* were also less abundant in *nbr1*, whereas 65-70% of the less abundant chloroplast proteins in *nbr1* showed reduced abundance in *atg7*, under both LL and HL conditions (Fig. 6C), further supporting that ATG7 and NBR1 control different aspects of chloroplast remodeling/turnover after HL. Remarkably, there was only a small overlap between the less abundant proteins in each mutant under LL and after HL treatment (Fig. 6D), suggesting that although chloroplast proteins are less abundant in the mutants under both light treatments, HL exposure triggered changes in the abundance of different sets of chloroplast proteins compared to LL conditions.

The observed relative decrease in chloroplast protein abundance in the three mutants was not a general trend for all organelles as might be expected if general autophagy was compromised. For example, the abundance of peroxisomal proteins were largely unchanged in *nbr1* but greater in *atg7* under HL compared to wild type (Fig. 6-figure supplement 2), consistent with a failure of the mutant to degrade damaged peroxisomes after HL exposure as previously reported in *atg7* plants (Oikawa et al., 2022).

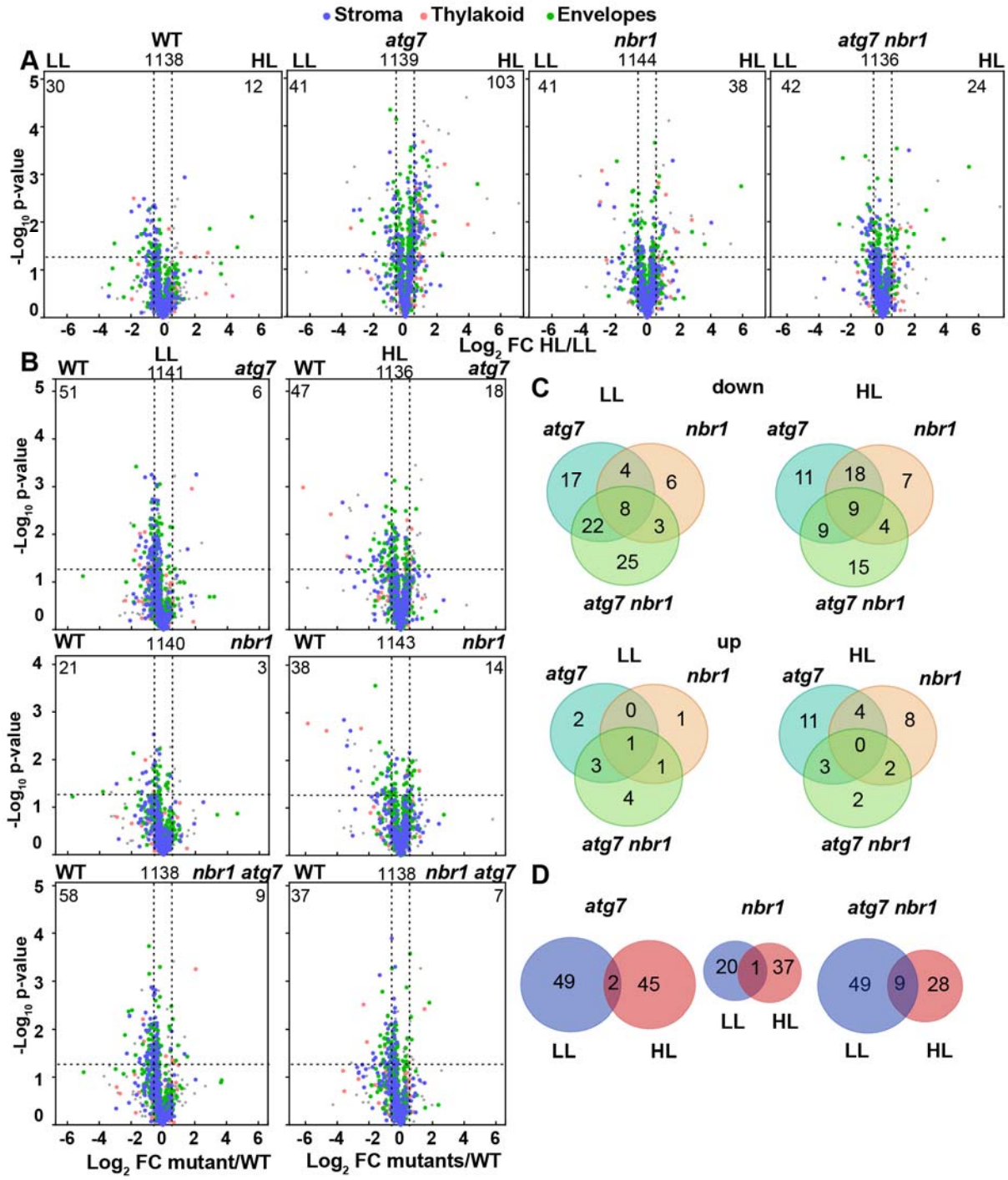

Figure 6. Chloroplast proteome analysis by liquid chromatography-tandem mass spectrometry (LC-MS/MS).

(A) Volcano plots showing the relative changes in chloroplast protein abundance in wild-type Col-0 (WT), *nbr1*, *atg7*, and *nbr1 atg7* seedlings grown either under LL or exposed to HL and let recover for 24 h. Proteins were identified by LC-MS/MS, and their average abundances calculated from the MS1 precursor ion intensities. Only proteins with at least two peptide spectral matches were considered in this analysis.

Each protein is plotted based on its Log_2 FC (>Log_2 0.6 or <Log_2 -0.6) in abundance (HL/LL) and its -log_{10} *p*-value (>-log_{10} 1.3) in significance based on the three biological replicates.
(B) Volcano plots showing the changes in the relative abundance of chloroplast proteins in mutants compared to wild type WT, under two different light conditions.
(C) Venn's diagrams depicting the overlap among chloroplast DAPs (either less or more abundant) in mutants compared to WT, either under LL or after HL exposure.
(D) Overlap of less abundant chloroplast proteins in *atg7*, *nbr1*, and *nbr1 atg7* compared to WT, either under LL or after HL exposure.

Contributions of NBR1 domains to chloroplast recruitment.

To identify the NBR1 domains that help NBR1 associate with photodamaged chloroplasts, we expressed in the *nbr1-1 background* several mutant versions of YFP-NBR1 missing key domain functions, such as NBR1-mPB1 with a point mutation (K11A) in the PB1 domain (Fig. 7A, B) that disrupts NBR1 oligomerization (Hafren et al., 2017), NBR1-mAIM with two point mutations in the AIM domain (W661A, I664A) that block interaction with ATG8 (Svenning et al., 2011; Hafren et al., 2017), and NBR1-ΔUBA2 missing the UBA2 domain (Fig. 7A, B) and therefore, unable to bind ubiquitin (Svenning et al., 2011; Hafren et al., 2018). All fluorescent NBR1 fusion proteins remained cytosolic under LL condition (Fig. 7B, C). After HL exposure, YFP-NBR1 associated with photodamaged chloroplasts as expected, either forming coats (average ~3% of chloroplasts; n= 28 fields) or localizing inside a small fraction of chloroplasts (average ~0.5% of chloroplasts; n= 28 fields) (Fig 7B, C). YFP-NBR1mPB also localized to photodamaged chloroplasts but almost exclusively to their interior (Fig. 7B, C). Thus, although the total percentages of chloroplasts labeled by YFP-NBR1 and YFP-NBR1mPB were similar (Fig 7C), YFP-NBR1 mainly coated the surface of chloroplasts whereas most of YFP-NBR1mPB was located to the chloroplast lumen. Just like YFP-NBR1, YFP-NBR1mAIM was mostly detected as chloroplast coats (Fig. 7B and C). Interestingly, YFP-NBR1ΔUBA2 failed to associate with chloroplasts after HL exposure (Fig. 7B, C). The expression of the same set of NBR1 mutated proteins resulted in a similar pattern of chloroplast association in the *atg7 nbr1* seedlings exposed to HL (Fig. 7-figure supplement 1). Thus, these results suggest the UBA2 domain is required for NBR1 chloroplast association whereas the PB1 domain negatively regulates NBR1 intra-chloroplast localization and/or promotes degradation of NBR1-filled chloroplasts.

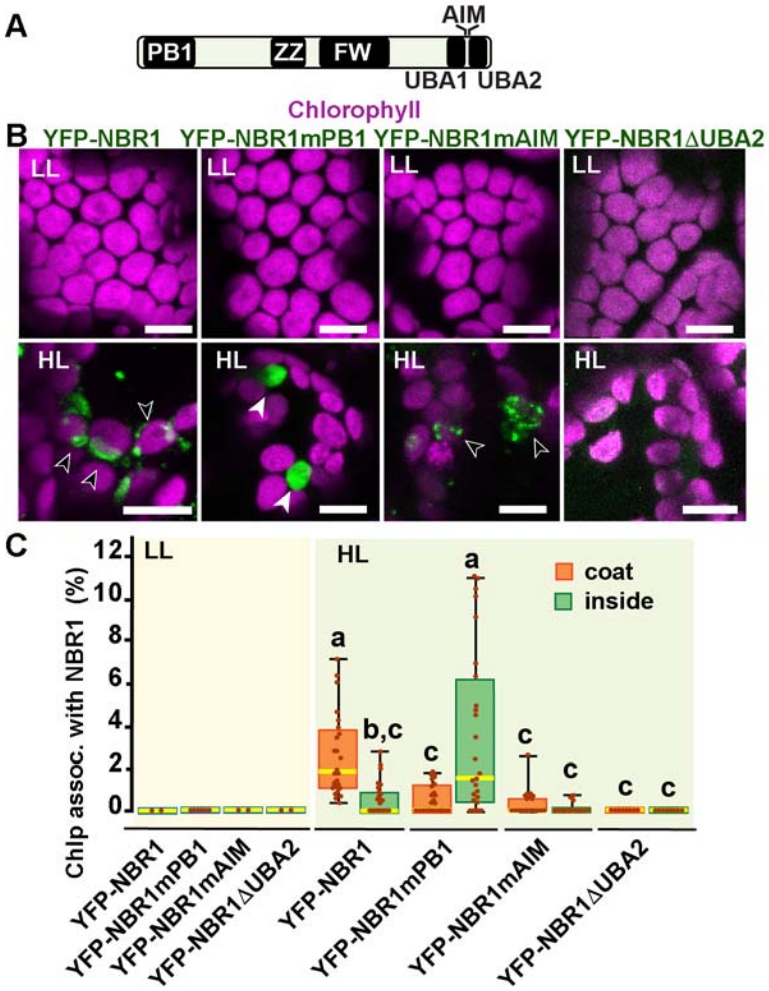

Figure 7. NBR1 domains have distinct roles in recruiting NBR1 to chloroplasts after HL treatment.

(A) Diagram of the Arabidopsis NBR1 protein and its domains. FW, Four-Tryptophan domain; PB1, Phox and Bem1p domain; ZZ, ZZ-type zinc finger domain; UBA1 and UBA2, ubiquitin-associated domains; AIM, ATG8-interacting motif.

(B) Confocal imaging of NBR1 mutated proteins fused to YFP expressed in 8-day-old *nbr1* seedlings grown under LL (top) or at 24 h after HL exposure (bottom). Hollow arrowheads and filled arrowheads indicate YFP-NBR1 coating chloroplasts and inside chloroplasts, respectively.

(C) Box and whisker plots show the percentages of chloroplast associated with the YFP-labeled mutated NBR1 proteins, localized to either coats (orange) or inside chloroplasts (green). Boxes show the variation in data through quartiles; the middle line indicates the median and whiskers show the upper and lower fences. Different letters denote significant differences from each other based on two-way ANOVA followed by Tukey's test ($p < 0.05$).

Scale bars: 10 μm in B.

485 **The E3 ligases PUB4 and SP1 are not required for NBR1 association with photodamaged**
486 **chloroplasts.**

487 Since the UBA2 ubiquitin-binding domain of NBR1 is critical for chloroplast association upon HL
488 treatment, we expressed NBR1-GFP in mutants lacking the E3 ligases PUB4 and SP1, which
489 have been shown to ubiquitylate chloroplast envelope proteins after photoradiation damage as
490 part of the CHLORAD pathway (Ling et al., 2012; Woodson et al., 2015). NBR1-GFP localized
491 to photodamaged chloroplasts in *pub4-2* and *sp1-2* single and double mutants during recovery
492 after HL (Fig. 8), suggesting that at least these two E3 ligases are not critical for NBR1
493 association with photodamaged chloroplasts.

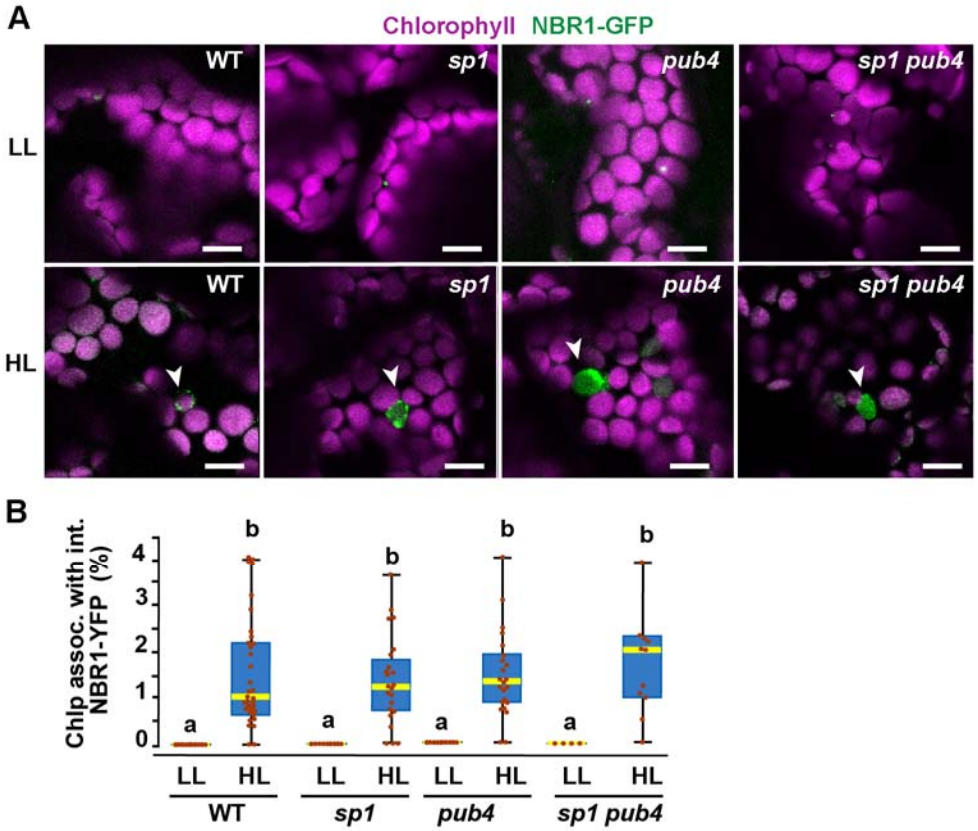

494

495 **Figure 8: NBR1 association with chloroplasts in mutants lacking SP1 and PUB4 E3**
496 **ligases.**

497 **(A)** Confocal imaging of NBR1-GFP in wild type (Col-0), *sp1*, *pub4*, and *sp1 pub4* 8-day old
498 seedlings under LL and 24 h after HL exposure. Arrowheads indicate chloroplasts decorated
499 with NBR1-GFP.

(B) Box and whisker plots show the percentage of chloroplast associated with NBR1-GFP under LL and 24 h after HL treatment. Boxes show the variation in data through quartiles; the middle line indicates the median and whiskers show the upper and lower fences. Different letters denote significant differences from each other based on two-way ANOVA followed by Tukey's test ($p < 0.05$).
Scale bar: 10 μm in A.

Fully functional TIC-TOC complexes are not required for NBR1 internalization into chloroplasts.

To test whether NBR1 is translocated into the chloroplast stroma *via* the TIC-TOC complexes, we expressed NBR1-GFP in the transcript-null *toc132-2* mutant, which is defective in the import of a subset of chloroplast proteins (Kubis et al., 2004). The *toc132-2* mutation did not affect the association of NBR1-GFP with chloroplasts or its localization into the chloroplast lumen (Fig. 9A, B).

As the *toc132-2* mutation affects the translocation of only some but not all chloroplast proteins into the stroma (Kubis et al., 2004), we also tested NBR1 localization in the transcript-knockout *tic40-4* mutant, which is severely deficient in chloroplast protein import and consistently develops structurally abnormal chloroplasts (Kovacheva et al., 2005). We isolated protoplasts from 3-week old *tic40-4* and wild-type seedlings and transfected them with the *pUBN-NBR1mPB1* vector, since the NBR1mPB1 protein is internalized into photodamaged chloroplasts at a higher rate than the wild-type NBR1 protein (Fig. 7C). We exposed the transfected protoplasts to HL for 2 h and imaged them 12 h later. We found that YFP-NBR1mPB1 successfully internalized into photodamaged chloroplasts in *tic40-4* mutant protoplasts. In fact, we detected a larger proportion of chloroplasts with internal YFP-NBR1mPB1 signal in the *tic40-4* compared to wild-type protoplasts (Fig 9. C, D). Taken together, these results suggest that the TIC-TOC complex is not required for the internalization of NBR1 into chloroplasts after HL exposure.

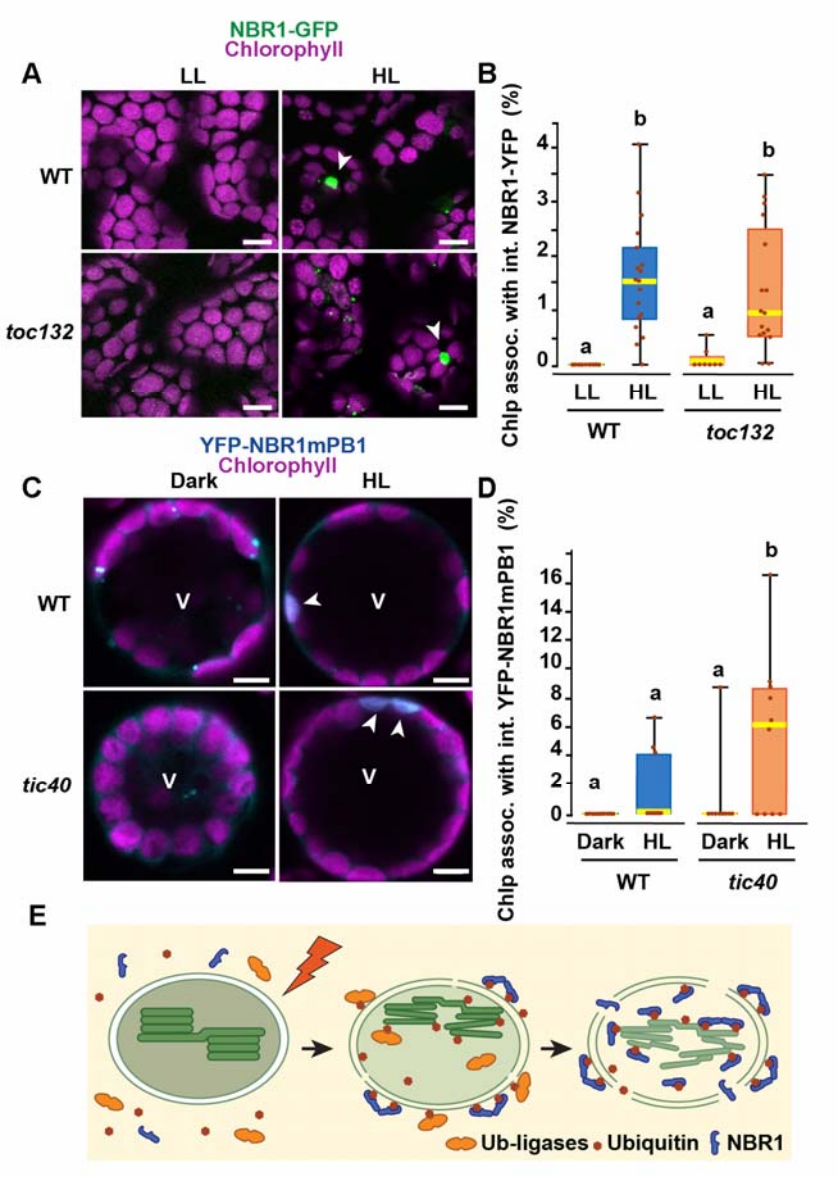

Figure 9. The TIC-TOC translocon is not required for the internalization of NBR1 into photodamaged chloroplasts.

(A) Confocal imaging of NBR1-GFP in wild-type Col-0 (WT) and *toc132* cotyledon mesophyll cells from 1-week old seedlings grown under LL or at 24 h after HL exposure. Arrowheads indicate chloroplasts with internal NBR1-GFP signal.

(B) Box and whisker plot displaying the percentages of chloroplasts associated with NBR1-GFP signal in WT and *toc132* mutant mesophyll cells under LL or at 24h after HL exposure. Between 9 and 18 confocal images of at least 3 cotyledons were used for quantification.

(C) Protoplasts from 3-week-old wild-type Col-0 (WT) and *tic40-4* expressing YFP-NBR1mPB1. Protoplasts were left in the dark or exposed to HL for 2 h and imaged 12 h later. Arrowheads indicate chloroplasts with internal YFP-mPB1-NBR1 signal. V, vacuole.

(D) Box and whisker plot displaying the percentages of wild type and *tic40-4* chloroplasts associated with YFP-mPB1-NBR1 signal in WT and *tic40-4* mutant protoplasts kept in dark conditions or exposed to HL and left to recover for 12 h. Between 9 and 10 protoplasts of each genotype and condition were used for quantification.

In B and D, boxes show the variation in data through quartiles; the middle line indicates the median and whiskers show the upper and lower fences. Different letters denote significant differences from each other based on two-way ANOVA followed by Tukey's test ($p < 0.05$).

(E) Diagram summarizing a proposed mechanism for NBR1 association with photodamaged chloroplasts. HL exposure induces the breakdown of the chloroplast envelopes allowing the cytosolic ubiquitylation machinery to reach the stroma and thylakoids of photodamaged chloroplasts. As stromal and thylakoidal proteins become ubiquitylated, NBR1 diffuses into damaged chloroplasts and bind ubiquitylated proteins through its UBA2 domain. NBR1-decorated photodamaged chloroplasts are then delivered to the vacuole by microautophagy independently of ATG7.

Scale bars: 5 µm in A and C.

Discussion

Here, we present evidence that the selective autophagy receptor NBR1 is recruited to photodamaged chloroplasts, mediating their clearance by a microautophagy-like event that is independent of the canonical ATG machinery (Figs. 1-4). Upon photoradiation damage, NBR1 first becomes associated with the chloroplast surface to be later internalized into the chloroplast stroma (Fig. 1E). The association of NBR1 with chloroplasts requires its ubiquitin-binding UBA2 domain whereas NBR1 internalization into the chloroplast stroma is negatively regulated by its self-polymerization PB1 domain (Fig. 7). The relocation of NBR1 into the chloroplast stroma does not rely on a functional TIC-TOC complex (Fig. 9). We hypothesize that the rupture of the outer and inner envelopes in photodamaged chloroplasts (Fig. 2C) allows for the diffusion of the ubiquitylation machinery and NBR1 from the cytosol into the chloroplast lumen, promoting ubiquitylation of both stroma and thylakoid proteins and their subsequent binding to NBR1 (Fig 9E).

NBR1 as a ubiquitin-binding chlorophagy receptor.

NBR1 is a well-known aggrephagy receptor that recognizes and sorts ubiquitylated cargo for vacuolar clearance (Rasmussen et al., 2022). In plants, the formation of ubiquitylated cargo aggregates by NBR1 depends on it self-oligomerizing PB1 domain and its ubiquitin-binding capacity through the UBA2 domain (Svenning et al., 2011; Zientara-Rytter and Sirko, 2014). The AIM domain of NBR1 mediates its interaction with ATG8 and its sequestration into autophagosomes for vacuolar degradation (Svenning et al., 2011). Our studies found that, upon high photoradiation exposure, NBR1 associates with a population of photodamaged chloroplasts via a process dependent on its UBA2 domain, which then enables the association of NBR1 with both the surface of the chloroplast and its lumen (stroma and thylakoids).

A simple scenario based on past studies is that NBR1 binds ubiquitylated substrates of the E3 ligases PUB4 and SP1, which ubiquitylate chloroplast envelope proteins as part of the CHLORAD pathway (Ling et al., 2012; Woodson et al., 2015). However, we found that a mutant lacking both PUB4 and SP1 activity showed normal recruitment of NBR1 to photodamaged chloroplasts (Fig. 8). Recent reports have shown that most chloroplast proteins, including those localized to stroma and thylakoids are ubiquitylated for subsequent break down by the proteasomes (Li et al., 2022; Sun et al., 2022b), but how such ubiquitylation might occur inside chloroplasts was unresolved. As rupture of the chloroplast envelope membranes is a known consequence of damaging photoradiation (Nakamura et al., 2018), it is important to note our observations that NBR1 heavily decorates the surface, stroma, and thylakoids of photodamaged chloroplasts with structurally disrupted envelopes (Fig. 2E, F). Consequently, we hypothesize that the loss of envelope structural integrity allows the cytosolic ubiquitylation machinery to access the stroma and thylakoid of compromised chloroplast thus directing the massive ubiquitylation of chloroplast proteins for recognition by the NBR1 receptor. Although ubiquitylation of intra-chloroplast proteins has been connected to degradation by the 26S proteasome through CHLORAD (Li et al., 2022; Sun et al., 2022b), it is possible that remaining ubiquitylated chloroplast ghost membranes coated with NBR1 are delivered to the vacuole by microautophagy.

The mPB1 domain of NBR1 is necessary for aggrephagy in plants as it mediates the formation of ubiquitylated cargo accretions (Svenning et al., 2011). Here, we show that an NBR1 protein unable to oligomerize is relocated into the chloroplast lumen at a higher frequency than the wild-type NBR1 protein (Fig. 7B, C). We hypothesize that monomeric NBR1 proteins can diffuse more easily through disrupted envelope membranes and reach the chloroplast stroma where they bind ubiquitylated chloroplast proteins.

Surprisingly, although NBR1 targets photodamage chloroplasts for vacuolar clearance, this process requires neither its ATG8-interacting AIM domain nor ATG7, and thus independent of canonical autophagy. Although microautophagy of ATG8-decorated chloroplasts upon radiation damage requires the core ATG machinery that assembles the ATG8-PE adduct (Izumi et al., 2017), microautophagy of chloroplasts damaged by oxidative stress does not (Lemke et al., 2021). Thus, as a protein targeting chloroplasts for non-canonical microautophagy, it is possible that NBR1 also mediates the clearance of chloroplast damaged by oxidative stress.

Autophagy defective maize (*atg12*) and Arabidopsis (*atg2*, *atg5*, *atg7*, and *atg9*) mutant plants show reduced abundance of chloroplast proteins in different developmental and environmental conditions (McLoughlin et al., 2018; Wijerathna-Yapa et al., 2021), despite autophagy being a catabolic pathway. This could be attributed to either a lower nutrient availability in autophagy defective lines, which results in lower protein biosynthesis, or the induction of alternative proteolytic pathways to compensate for the lack of autophagy. Here, in the absence of nutritional deficiency, we also observed a lower abundance of chloroplast proteins for all autophagy defective lines (*atg7*, *nbr1*, and *nbr1 atg7*) after HL exposure (Fig 6B), consistent with either the induction of other proteolytic route(s) and/or a delay in chloroplast protein synthesis and recovery after photoradiation damage. In this context, both *nbr1* and *nbr1 atg7* plants, showed a lessened reduction in chloroplast protein abundance relative to *atg7* (Fig 6B). We speculate that all these lines display enhanced degradation of chloroplast proteins, but mutations in *NBR1* dampen this exacerbated catabolic activity that target chloroplasts when autophagy is blocked.

The role of NBR1 in organelle turnover and remodeling does not seem to be general for all organelles as peroxisomal protein abundance was not altered in *nbr1* backgrounds but significantly elevated in the *atg7* mutant (Fig. 6-figure supplement 2). This also confirms previous reports that, different from animals (Deosaran et al., 2013), plants do not seem to employ NBR1 for autophagic removal of peroxisomes (pexophagy) (Young et al., 2019; Jung et al., 2020).

The many pathways promoting chloroplast remodeling and degradation.

Chloroplast proteostasis is critical for plant survival, which is constantly challenged by daily exposure to damaging reactive oxygen species generated by the photosynthetic machinery (Foyer, 2018) and by a hypersensitivity of chloroplasts to biotic and abiotic stresses (Nishimura et al., 2017; Song et al., 2021; Wang et al., 2022). A failure to control chloroplast

635 protein turnover is often very deleterious to plants (Rowland et al., 2022). Not surprisingly
636 considering the complexity of the organelle and its functions, chloroplast remodeling and
637 turnover are intricate processes that integrates multiple and likely redundant or partially
638 redundant pathways. Besides chloroplast proteases that can locally degrade proteins inside
639 chloroplasts (Nishimura et al., 2017; Rowland et al., 2022), several autophagy and non-
640 autophagic pathways mediate vacuolar clearance of chloroplast components (Otegui, 2018;
641 Kikuchi et al., 2020; Rowland et al., 2022). At least three flavors of ATG8-dependent piecemeal
642 autophagy of chloroplasts have been characterized: Rubisco-containing bodies (Chiba et al.,
643 2003; Ishida et al., 2008; Spitzer et al., 2015), ATG8-INTERACTING PROTEIN 1 bodies
644 (Michaeli et al., 2014), and small starch-like granule bodies (Wang et al., 2013). In addition,
645 microautophagy of whole damaged chloroplasts occurs through at least two pathways, one
646 dependent and the other independent of canonical autophagy (Izumi et al., 2017; Lemke et al.,
647 2021). For the latter pathway, we provide evidence for a novel microautophagic route that
648 requires NBR1 but not ATG8 lipidation.

649 How exactly all these pathways coordinate the remodeling and degradation of damaged
650 chloroplasts is unclear. Upon HL exposure, we observed chloroplasts associated with either
651 ATG8 and NBR1 as organelle cargo for canonical autophagy-dependent and independent
652 microautophagy, respectively (Fig. 3). Only a very low proportion of chloroplasts were coated
653 with both ATG8 and NBR1, supporting the notion that there are two separate microautophagy
654 pathways for chloroplast clearance. However, we noticed a higher proportion of NBR1-
655 decorated chloroplasts in HL-exposed *atg7* mutant seedlings compared to controls (Figs. 1F
656 and 4C), consistent with the idea that photodamaged chloroplasts that are not successfully
657 repaired or degraded by canonical autophagy, become substrates of NBR1. Interestingly, the
658 *tic40-4* mutant that contains structurally abnormal chloroplasts (Kovacheva et al., 2005) also
659 shows increased association of chloroplasts with NBR1 upon HL exposure (Fig. 9C), consistent
660 with more widespread photodamage in the *tic40-4* chloroplasts, which in turn results in more
661 chloroplasts being targeted by NBR1.

662 We had anticipated that an *nbr1 atg7* double mutant exposed to HL would show more
663 pronounced defects in chloroplast homeostasis after HL exposure than the single mutants if the
664 ATG8- and NBR1-mediated microautophagy pathways were both disrupted. However, the *nbr1*
665 *atg7* double mutant did not show more drastic phenotypic alterations as compared to those
666 seen in the single mutants in terms of both chlorophyll mean intensities and chloroplast
667 proteome profiles, and instead, the mutant behaves either as intermediate between the two

668 single mutants or more similarly to the *atg7* single mutant. This disconnection suggests that
669 canonical autophagy controls the main pathway for clearance of photodamaged chloroplasts,
670 whereas NBR1 targets a relatively small population of chloroplasts and chloroplast proteins that
671 fail to be degraded via either CHLORAD or canonical autophagy.

672

673 **Methods and Materials**

674 **Plant materials and growth conditions**

675 *Arabidopsis thaliana* seeds of *atg7-2* (GABI_655B06) (Chung et al., 2010), *nbr1-1*
676 (SALK_135513) (Zhou et al., 2013), *nbr1-2* (GABI_246H08) (Zhou et al., 2013), *atg7-2 nbr1-2*
677 (Jung et al., 2020), *toc132-2* (SAIL_667_04) (Kubis et al., 2004), *tic40-4* (SAIL_192_C10)
678 (Kovacheva et al., 2005), *Pro35S:mCherry-NBR1* (Svenning et al., 2011), ProUBQ10:mCherry-
679 NBR1 (Jung et al., 2020), *ProNBR1:NBR1-GFP* (Hafren et al., 2017; Thirumalaikumar et al.,
680 2021), *Pro35S:RECA-GFP* (Kohler et al., 1997; Spitzer et al., 2015) were previously
681 characterized. The *sp1-2* (SALK_063571) (Ling et al., 2012) and *pub4-2* (SALK_054373)
682 (Woodson et al., 2015) mutant lines were acquired from Arabidopsis Biological Resource Center
683 (https://abrc.osu.edu/) and *sp1-2 pub4*-2 *ProNBR1:NBR1-GFP* was generated by crossing.
684 Primers used for genotyping the lines above are listed in Supplemental table 14.

685 To fuse YFP to NBR1 mutant variants, NBR1, NBR1mPB, NBR1mAIM, and
686 NBR1ΔUBA2 were cloned into the Gateway entry vector pDONR221 by the BP Clonase II
687 reactions (Thermo Fisher Scientific) using Gateway expression vectors previously described
688 (Hafren et al., 2017). The resulting entry clones were recombined with pUBN-DEST-YFP
689 (Grefen et al., 2010) via the LR Clonase II reaction (Thermo Fisher Scientific) to generate the
690 expression vectors with YFP. The sequences were confirmed by Sanger sequencing with YFP
691 and NBR1 primers. The expression vectors were introduced into *Agrobacterium tumefaciens*
692 strain GV3101. *Agrobacterium* transformants were used to transform *nbr1-2* or *atg7-2 nbr1-2*
693 mutants by the floral dip method (Clough and Bent, 1998). T1 plants were selected on the
694 media supplemented with 10 mg/L Basta.

695 Seeds were surface-sterilized in 10% (v/v) bleach and 1% (v/v) Triton X-100 solution for
696 30 min and washed in distilled water at least five times. Seeds were sown on solid media
697 containing 0.5x Murashige & Skoog salts (MS), 1% (w/v) sucrose and 0.6% Phytagel and
698 stratified at 4℃ for 2-5 days before germination. Plants were grown in growth chambers at 22ºC
699 under 16 h of light (40 µmol m^{-2} s^{-1}) and 8 h of dark cycle (LL). For high-light treatment (HL), 8-

d-old seedlings were exposed to 2000 W LED lights (1500 µmol m^{-2} s^{-1}) at 12ºC for 2 hours followed by recovery for the indicated time.

Transient expression in Arabidopsis leaf protoplasts

Isolation and transformation of Arabidopsis leaf protoplasts were performed as previously described (Yoo et al., 2007) with some modifications. Briefly, rosette leaves from 3-week-old Arabidopsis wild type (Col-0) and *tic40-4* (Kovacheva et al., 2005) plants were used for protoplast isolation. Protoplasts were released in enzyme solution (20 mM MES pH 5.7, 1.5% [w/v] cellulase R10, 0.4% [w/v] macerozyme R10, 0.4 M mannitol and 20 mM KCl, 10 mM CaCl2, and 0.1% BSA) for 1 h and collected by centrifugation at 100 g for 5 min. Protoplasts were washed twice with W5 buffer (2 mM MES [pH 5.7] containing 154 mM NaCl, 125 mM CaCl2 and 5 mM KCl). Then, 7 µg of the *pUBN-YFP-NBR1mPB* vector was used for each transformation with polyethylene glycol. After transformation, the protoplasts were incubated at 22 ºC under dark for 2 h. For HL treatment, the transformed protoplasts were exposed to 1,500 µmol m^{-2} s^{-1} at 12ºC for 2 h followed by recovery in the dark at 22ºC. Control protoplasts were kept under dark conditions at 22 ºC until imaging.

For confocal imaging, protoplasts were loaded onto an 18 Well Flat m-Slide (Ibidi). Images were captured on a Zeiss LSM 780 confocal microscope with a 63x water immersion objective. YFP was excited with a 488 nm laser and detected using a 493–527 nm band-pass filter; chlorophyll was excited with a 633 nm laser and detected using a 642–695 nm band-pass filter. Between 9 and 10 protoplasts were used for quantification of each condition and phenotype.

Light microscopy and image analysis

Confocal images were obtained in a Zeiss LSM 710 with a 40x objective (LD C-Apochromat NA = 1.2 water immersion, Carl Zeiss). GFP, YFP, and chlorophyll were excited using a 488 nm laser and emission was collected from 450 to 560 nm for GFP/YFP and from 650 to 710 nm for chlorophyll. mCherry was excited using a 561 nm laser and emission collected from 570 to 640 nm. Quantification of confocal images was done with FIJI (Schindelin et al., 2012). To verify the specificity of the fluorescence signals, the emission spectra resulting from 488-nm excitation were collected between 420 and 720 nm using the lambda scan mode.

Multiphoton images were collected using a Nikon 40x water-immersion objective lens (1.25 NA, CFI Apochromat Lambda S 40XC WI) on an Ultima IV multiphoton microscope (Bruker FM). Chlorophyll was imaged using 890 nm multiphoton excitation from an Insight laser (Spectra Physics) and fluorescence emission was filtered using a dichroic cube filter set (720nm, 630/69 nm, Chroma Technologies). Using manual estimation of leaf size and volumetric scanning from the surface to 100 microns deep, regions of interests were chosen and imaged. A hybrid photomultiplier tube (HPM-40, Becker&Hickl GmbH) detector was deployed in photon counting mode using a fast electronic board (SPC-150, Becker&Hickl GmbH), and Prairie View (Bruker FM) software. In presence of GFP markers, a second channel was imaged using a bialkali detector with 535/50 filter (Chroma Technologies).

The fluorescence images were made to 2D, using a maximum intensity projection and then 2D segmentation methods were applied to identify single chloroplasts. Cellpose 2.0.5 (Nucleus-model) with GPU acceleration (NVIDIA GeForce RTX 2080 Ti) generated robust chloroplast masks, which were then processed using Python (v3.9.12, Python Software Foundation) to calculate single chloroplast intensity and other morphological traits (Stringer et al., 2021)

Protein preparation for western blots

Whole 8-day-old Arabidopsis seedlings were frozen with liquid nitrogen and homogenized in protein extraction buffer (150 mM Tris-HCl (pH7.5), 150 mM NaCl, 10 mM $MgCl_2$, 10% [v/v] glycerol, 2% [w/v] polyvinylpyrrolidone, 3 mM dithiothreitol, 2 mM phenylmethylsulfonyl fluoride, 0.1% [v/v] Triton X-100, 1x protease inhibitor cocktail), and centrifuged at 25,000 g for 10 min at 4°C. The supernatants were mixed with 0.25 volumes of 5x SDS-PAGE sample buffer containing 10% [v/v] 2-mercaptoethanol and boiled before subjecting them to SDS-PAGE gel followed by immunoblotting with the indicated antibodies.

Protein preparation for mass spectrometry (MS) analysis.

Seven-day-old wild type (Col-0), *nbr1-2*, *atg7-2*, and *nbr1-2 atg7-2* Arabidopsis seedlings were either grown under LL or left to recover for 24h after HL exposure as explained above. Whole seedlings were frozen in liquid nitrogen and grinded; protein extraction buffer (50 mM HEPES pH7.5, 5 mM Na_2 EDTA, 2mM DTT, 1x protease inhibitor cocktail) was added to the samples. After mixing, samples were left on ice for 15 min, and transferred to a homogenizer for gentle

764 homogenization. The homogenate was left on ice for 15 min and centrifuged at 14,000 g for 1
765 min at 4°C; 150 µL of the supernatant was transferred to clean 1.5mL plastic tubes, mixed well
766 by vortexing with 600 µL methanol and 150 µL chloroform. Then, 450 µL milliQ water was
767 added to the sample and mixed by vortexing, followed by centrifugation at 14,000 g for 2 min.
768 The top aqueous layer was removed and the proteins in the interphase collected with a pipette
769 and transferred to a clean plastic tube followed by addition of 400 µL methanol, vortexing, and
770 centrifugation at 14,000 g for 3 min. Methanol was removed from the tube without disturbing the
771 pellet, which was left to dry in a vacuum concentrator.

772

773 **Liquid chromatography-tandem MS (LC-MS/MS).**

774 Protein pellets were resuspended in 100 µL of 8M urea. Then,100 ug protein of each sample
775 was reduced for 1h at room temperate with 10 mM dithiothreitol, followed by alkylation with 20
776 mM iodoacetamide (IAA) for 1h. The reaction was quenched with 20 mM dithiothreitol (DTT)
777 and diluted with 900 µL 25 mM ammonium bicarbonate to reduce the urea concentration below
778 1 M, digested overnight at 37°C in the presence of 1.5 µg of sequencing grade modified trypsin
779 (Promega). The resulting peptides were vacuum-dried in a vacuum concentrator to
780 approximately 200 µL, acidified with 10% trifluoroacetic acid (TFA) (pH < 3), desalted and
781 concentrated on a 100-µL Bond Elut OMIX C18 pipette tip (Agilent Technologies A57003100)
782 according to the manufacturer's instructions. Peptides were eluted in 50 µL of 75% acetonitrile,
783 0.1% acetic acid, vacuum-dried, and resuspended in 15 µL 5% acetonitrile, 0.1% formic acid.

784 Nanoscale liquid chromatography (LC) separation of tryptic peptides was performed on a
785 Dionex Ultimate 3000 Rapid Separation LC system (Thermo Fisher). Peptides were loaded
786 onto a 20 µL nanoViper sample loop (Thermo Fisher) and separated on a C18 analytical column
787 (Acclaim PepMap RSLC C18 column, 2 µm particle size, 100 Å pore size, 75 µm × 25 cm,
788 Thermo Fisher) by the application of a linear 2 h gradient from 4% to 45% acetonitrile in 0.1%
789 formic acid, with a column flow rate set to 250 nL/min. Analysis of the eluted tryptic peptides
790 was performed online using a Q Exactive Plus mass spectrometer (Thermo Scientific)
791 possessing a Nanospray Flex Ion source (Thermo Fisher) fitted with a stainless steel nano bore
792 emitter operated in positive electrospray ionization (ESI) mode at a capillary voltage of 1.9 kV.
793 Data-dependent acquisition of full MS scans within a mass range of 380–1500 m/z at a
794 resolution of 70,000 was performed, with the automatic gain control (AGC) target set to $3.0 \times$
795 10^6, and the maximum fill time set to 200 ms. High-energy collision-induced dissociation (HCD)
796 fragmentation of the top eight most intense peaks was performed with a normalized collision

energy of 28, with an intensity threshold of 4.0×10^4 counts and an isolation window of 3.0 m/z, excluding precursors that had an unassigned, +1 or >+7, charge state. MS/MS scans were conducted at a resolution of 17,500, with an AGC target of 2×10^5 and a maximum fill time of 300 ms. The resulting MS/MS spectra were analyzed using Proteome Discoverer software (version 2.5, Thermo Fisher), which was set up to search the *A. thaliana* proteome database, as downloaded from http://www.tair.com/ (Araport11_pep_20220914). Peptides were assigned using SEQUEST HT (Eng et al., 1994), with search parameters set to assume the digestion enzyme trypsin with a maximum of 1 missed cleavage, a minimum peptide length of 6, precursor mass tolerances of 10 ppm, and fragment mass tolerances of 0.02 Da. Carbamidomethylation of cysteine was specified as a static modification, while oxidation of methionine and N-terminal acetylation were specified as dynamic modifications. The target false discovery rate (FDR) of 0.01 (strict) was used as validation for peptide-spectral matches (PSMs) and peptides. Proteins that contained similar peptides and that could not be differentiated based on the MS/MS analysis alone were grouped to satisfy the principles of parsimony. Label-free quantification as previously described (Silva et al., 2006) was performed in Proteome Discoverer with a minimum Quan value threshold of 0.0001 using unique peptides, and '3 Top N' peptides used for area calculation. All samples were injected in two technical duplicates, and the protein abundances reflected the average of two technical replicates if proteins were detected in two technical replicates or used directly if the proteins were only detected in one technical replicate. Protein abundances were normalized using the median values of 150 proteins considered the least variable among each sample. The mass spectrometry proteomics data have been deposited to the ProteomeXchange Consortium *via* the PRIDE partner repository (Perez-Riverol et al., 2019) with the dataset identifier PXD039183.

Using the Perseus platform (Tyanova et al., 2016), intensity values from mass spectrometry were $\log_2$ mputed and missing values were replaced with random numbers from a Gaussian distribution with a width of 0.3 and a downshift of 1.8. Statistical significance was determined using *t*-tests. Only proteins with at least 2 peptide spectral matches (one is the unique peptide) were selected for further analysis.

Electron microscopy and immunogold labeling.

Wild type (Col-0), *atg7-2*, and *nbr1-2* seedlings were germinated in liquid media containing 0.5x MS and 1% sucrose. Eight-day-old cotyledons either grown under LL or at 24 h after HL exposure were cut into small pieces and frozen in a high-pressure freezer (Leica EM Ice). To

analyze the ultrastructure of chloroplasts, the samples were freeze-substituted in 2% (w/v) osmium tetroxide in acetone on dry ice overnight; samples were adjusted to room temperature on a rocker. After several rinses with acetone, the samples were infiltrated with Epon resin (Electron Microscopy Sciences) with increasing the concentration of Epon 10% (v/v), 25%, 50%, 75% in acetone, followed by three exchanges with 100% Epon. The samples were embedded and polymerized at 60°C for 24 h. For immunogold labeling, the high-pressure-frozen samples were freeze-substituted in 0.2% glutaraldehyde with 0.2% uranyl acetate in acetone at -90°C in an automated freeze-substitution device (Leica AFS). After 3 days, the temperature was raised at 5°C/h to -60°C and the samples were rinsed with precooled acetone three times and infiltrated with 30%, 60%, and 100% HM20 (Electron Microscopy Sciences) in acetone and polymerized under UV light at -50ºC. Sections were blocked with 5% (w/v) solution of nonfat milk in PBS (phosphate buffered saline) containing 0.1% Tween-20 (blocking solution) for 20 min, incubated with anti-NBR1 antibodies in the blocking solution (1:10) for 1 h, rinsed 3 times with PBS containing 0.5% Tween-20, and incubated with anti-rabbit secondary antibody conjugated to gold particles (Electron Microscopy Sciences) in the blocking solution for 1 h. After 3 rinses with the PBS containing 0.5% Tween-20 and another rinse with water, the samples were imaged with a transmission electron microscope (Thermo Fisher Scientific Talos).

Chloroplast isolation.

Intact chloroplasts were isolated as previously described with some modifications (Kley et al., 2010; Lung et al., 2015). Four-week-old leaves were punched repeatedly with a 1 ml pipette tip in buffer (0.3 M sorbitol, 50 mM HEPES/KOH [pH 7.5], 5 mM ethylenediaminetetraacetic acid [EDTA], 5 mM ethyleneglycoltetraacetic acid [EGTA], 1 mM $MgCl_2$, 10 mM $NaHCO_3$, and 0.5 mM dithiothreitol) and filtered through cheesecloth. The filtrate was carefully loaded onto a two-step Percoll gradient that was prepared by overlaying 40% Percoll buffer on top of 85% Percoll and centrifuged for 20 min at 2,000 g in a swing out rotor, brakes set off. The upper layer of the 40% Percoll containing broken chloroplasts was discarded, and the intact chloroplasts at the interface of the Percoll layers was collected and washed 5 times by adding buffer and centrifuged for 5 min at 1,000 g. Isolated chloroplasts were resuspended in buffer. We then added 0.25 volumes of 5x SDS-PAGE sample buffer containing 10% (v/v) 2-mercaptoethanol to the samples. Protein extracts were subjected to SDS-PAGE followed by immunoblotting with the indicated antibodies.

Antibodies

Antibodies against GFP (Chromotek), anti-PsbA/D1 (Agrisera), anti-cFBPase (Agrisera AS04043), anti-TIC40 (Agrisera), anti-Toc75 (Agrisera), anti-NBR1 (Jung et al., 2020), and histone H3 (Abcam AB1791) were obtained from the indicated sources.

Statistical analyses

T-tests were performed in Microsoft Excel. ANOVA tests followed by post-hoc Tukey were performed using the calculator at https://astatsa.com/OneWay_Anova_with_TukeyHSD/. Data was visualized using GraphPad Prism 9 and Excel. The Venn diagram shown in Fig 6 were created using http://bioinformatics.psb.ugent.be/webtools/Venn/.

Accession numbers: NBR1 (At4g24690), ATG7 (At5g45900), SP1 (At1g63900), PUB4 (At2g23140), TOC132 (At2g16640), TIC40 (AT5G16620).

Materials availability: newly generated transgenic lines are available upon request.

Funding: This work was supported by grants U.S. National Science Foundation IOS-1840687 to M.S.O. and R.D.V., U.S. Department of Energy grant DE-SC0019013 to MSO and KWE, National Institute of Health 1S10 OD026769-01 to MSO, and Australian Research Council (FL200100057) to AHM.

Acknowledgements: We would like to thank Daniel Hofius for sharing NBR1 constructs with us, Taijoon Chung for providing mutant and transgenic lines, Janice Pennington for her assistance with the electron microscopy analysis, and Dr Sarah Swanson for her support with confocal imaging.

Competing interests: the authors declare no competing interests.

References

Bjørkøy, G., Lamark, T., Brech, A., Outzen, H., Perander, M., Overvatn, A., Stenmark, H., and Johansen, T. (2005). p62/SQSTM1 forms protein aggregates degraded by

894 autophagy and has a protective effect on huntingtin-induced cell death. J Cell Biol **171,**
895 603-614.
896 **Cha-Molstad, H., Sung, K.S., Hwang, J., Kim, K.A., Yu, J.E., Yoo, Y.D., Jang, J.M., Han,**
897 **D.H., Molstad, M., Kim, J.G., Lee, Y.J., Zakrzewska, A., Kim, S.H., Kim, S.T., Kim,**
898 **S.Y., Lee, H.G., Soung, N.K., Ahn, J.S., Ciechanover, A., Kim, B.Y., and Kwon, Y.T.**
899 (2015). Amino-terminal arginylation targets endoplasmic reticulum chaperone BiP for
900 autophagy through p62 binding. Nat Cell Biol **17,** 917-929.
901 **Chiba, A., Ishida, H., Nishizawa, N.K., Makino, A., and Mae, T.** (2003). Exclusion of ribulose-
902 1,5-biphosphate carboxylase/oxygenase from chloroplasts by specific bodies in naturally
903 senescing leaves of wheat. Plant Cell Physiol. **44,** 914-921.
904 **Chung, T., Phillips, A.R., and Vierstra, R.D.** (2010). ATG8 lipidation and ATG8-mediated
905 autophagy in *Arabidopsis* require ATG12 expressed from the differentially controlled
906 *ATG12A* and *ATG12B* loci. Plant J **62,** 483-493.
907 **Ciuffa, R., Lamark, T., Tarafder, A.K., Guesdon, A., Rybina, S., Hagen, W.J., Johansen, T.,**
908 **and Sachse, C.** (2015). The selective autophagy receptor p62 forms a flexible
909 filamentous helical scaffold. Cell Rep **11,** 748-758.
910 **Clough, S.J., and Bent, A.F.** (1998). Floral dip: a simplified method for Agrobacterium-
911 mediated transformation of *Arabidopsis thaliana*. Plant J **16,** 735-743.
912 **Dagdas, Y.F., Pandey, P., Tumtas, Y., Sanguankiattichai, N., Belhaj, K., Duggan, C., Leary,**
913 **A.Y., Segretin, M.E., Contreras, M.P., Savage, Z., Khandare, V.S., Kamoun, S., and**
914 **Bozkurt, T.O.** (2018). Host autophagy machinery is diverted to the pathogen interface to
915 mediate focal defense responses against the Irish potato famine pathogen. Elife **7,**
916 37476.
917 **Dagdas, Y.F., Belhaj, K., Maqbool, A., Chaparro-Garcia, A., Pandey, P., Petre, B.,**
918 **Tabassum, N., Cruz-Mireles, N., Hughes, R.K., Sklenar, J., Win, J., Menke, F.,**
919 **Findlay, K., Banfield, M.J., Kamoun, S., and Bozkurt, T.O.** (2016). An effector of the
920 Irish potato famine pathogen antagonizes a host autophagy cargo receptor. Elife **5,**
921 e10856.
922 **Deosaran, E., Larsen, K.B., Hua, R., Sargent, G., Wang, Y., Kim, S., Lamark, T., Jauregui,**
923 **M., Law, K., Lippincott-Schwartz, J., Brech, A., Johansen, T., and Kim, P.K.** (2013).
924 NBR1 acts as an autophagy receptor for peroxisomes. J Cell Sci **126,** 939-952.
925 **Eng, J.K., McCormack, A.L., and Yates, J.R.** (1994). An approach to correlate tandem mass
926 spectral data of peptides with amino acid sequences in a protein database. J Am Soc
927 Mass Spectrom **5,** 976-989.

928 **Foyer, C.H.** (2018). Reactive oxygen species, oxidative signaling and the regulation of
929 photosynthesis. Environ Exp Bot **154,** 134-142.
930 **Geldner, N., Denervaud-Tendon, V., Hyman, D.L., Mayer, U., Stierhof, Y.D., and Chory, J.**
931 (2009). Rapid, combinatorial analysis of membrane compartments in intact plants with a
932 multicolor marker set. Plant J **59,** 169-178.
933 **Grefen, C., Donald, N., Hashimoto, K., Kudla, J., Schumacher, K., and Blatt, M.R.** (2010). A
934 ubiquitin-10 promoter-based vector set for fluorescent protein tagging facilitates temporal
935 stability and native protein distribution in transient and stable expression studies. Plant J
936 **64,** 355-365.
937 **Hafren, A., Macia, J.L., Love, A.J., Milner, J.J., Drucker, M., and Hofius, D.** (2017). Selective
938 autophagy limits cauliflower mosaic virus infection by NBR1-mediated targeting of viral
939 capsid protein and particles. Proc Natl Acad Sci U S A **114,** E2026-E2035.
940 **Hafren, A., Ustun, S., Hochmuth, A., Svenning, S., Johansen, T., and Hofius, D.** (2018).
941 Turnip mosaic virus counteracts selective autophagy of the viral silencing suppressor
942 HCpro. Plant Physiol **176,** 649-662.
943 **Ichimura, Y., Kumanomidou, T., Sou, Y.S., Mizushima, T., Ezaki, J., Ueno, T., Kominami,**
944 **E., Yamane, T., Tanaka, K., and Komatsu, M.** (2008). Structural basis for sorting
945 mechanism of p62 in selective autophagy. J Biol Chem **283,** 22847-22857.
946 **Ishida, H., Yoshimoto, K., Izumi, M., Reisen, D., Yano, Y., Makino, A., Ohsumi, Y., Hanson,**
947 **M.R., and Mae, T.** (2008). Mobilization of Rubisco and stroma-localized fluorescent
948 proteins of chloroplasts to the vacuole by an ATG gene-dependent autophagic process.
949 Plant Physiol **148,** 142-155.
950 **Izumi, M., Ishida, H., Nakamura, S., and Hidema, J.** (2017). Entire photodamaged
951 chloroplasts are transported to the central vacuole by autophagy. Plant Cell **29,** 377-394.
952 **Jakobi, A.J., Huber, S.T., Mortensen, S.A., Schultz, S.W., Palara, A., Kuhm, T., Shrestha,**
953 **B.K., Lamark, T., Hagen, W.J.H., Wilmanns, M., Johansen, T., Brech, A., and**
954 **Sachse, C.** (2020). Structural basis of p62/SQSTM1 helical filaments and their role in
955 cellular cargo uptake. Nat Commun **11,** 440.
956 **Ji, C., Zhou, J., Guo, R., Lin, Y., Kung, C.H., Hu, S., Ng, W.Y., Zhuang, X., and Jiang, L.**
957 (2020). AtNBR1 Is a Selective Autophagic Receptor for AtExo70E2 in Arabidopsis. Plant
958 Physiol **184,** 777-791.
959 **Jung, H., Lee, H.N., Marshall, R.S., Lomax, A.W., Yoon, M.J., Kim, J., Kim, J.H., Vierstra,**
960 **R.D., and Chung, T.** (2020). Arabidopsis cargo receptor NBR1 mediates selective
961 autophagy of defective proteins. J Exp Bot **71,** 73-89.

962 **Kikuchi, Y., Nakamura, S., Woodson, J.D., Ishida, H., Ling, Q., Hidema, J., Jarvis, R.P.,**
963 **Hagihara, S., and Izumi, M.** (2020). Chloroplast autophagy and ubiquitination combine
964 to manage oxidative damage and starvation responses. Plant Physiol **183,** 1531-1544.
965 **Kley, J., Heil, M., Muck, A., Svatos, A., and Boland, W.** (2010). Isolating intact chloroplasts
966 from small Arabidopsis samples for proteomic studies. Anal Biochem **398,** 198-202.
967 **Kohler, R.H., Cao, J., Zipfel, W.R., Webb, W.W., and Hanson, M.R.** (1997). Exchange of
968 protein molecules through connections between higher plant plastids. Science **276,**
969 2039-2042.
970 **Komatsu, M., Waguri, S., Koike, M., Sou, Y.S., Ueno, T., Hara, T., Mizushima, N., Iwata, J.,**
971 **Ezaki, J., Murata, S., Hamazaki, J., Nishito, Y., Iemura, S., Natsume, T., Yanagawa,**
972 **T., Uwayama, J., Warabi, E., Yoshida, H., Ishii, T., Kobayashi, A., Yamamoto, M.,**
973 **Yue, Z., Uchiyama, Y., Kominami, E., and Tanaka, K.** (2007). Homeostatic levels of
974 p62 control cytoplasmic inclusion body formation in autophagy-deficient mice. Cell **131,**
975 1149-1163.
976 **Kovacheva, S., Bédard, J., Patel, R., Dudley, P., Twell, D., Ríos, G., Koncz, C., and Jarvis,**
977 **P.** (2005). In vivo studies on the roles of Tic110, Tic40 and Hsp93 during chloroplast
978 protein import. Plant J **41,** 412-428.
979 **Kubis, S., Patel, R., Combe, J., Bédard, J., Kovacheva, S., Lilley, K., Biehl, A., Leister, D.,**
980 **Ríos, G., Koncz, C., and Jarvis, P.** (2004). Functional specialization amongst the
981 Arabidopsis Toc159 family of chloroplast protein import receptors. Plant Cell **16,** 2059-
982 2077.
983 **Kwon, D.H., Park, O.H., Kim, L., Jung, Y.O., Park, Y., Jeong, H., Hyun, J., Kim, Y.K., and**
984 **Song, H.K.** (2018). Insights into degradation mechanism of N-end rule substrates by
985 p62/SQSTM1 autophagy adapter. Nat Commun **9,** 3291.
986 **Lemke, M.D., Fisher, K.E., Kozlowska, M.A., Tano, D.W., and Woodson, J.D.** (2021). The
987 core autophagy machinery is not required for chloroplast singlet oxygen-mediated cell
988 death in the Arabidopsis thaliana plastid ferrochelatase two mutant. BMC Plant Biol **21,**
989 342.
990 **Leong, J.X., Raffeiner, M., Spinti, D., Langin, G., Franz-Wachtel, M., Guzman, A.R., Kim,**
991 **J.G., Pandey, P., Minina, A.E., Macek, B., Hafrén, A., Bozkurt, T.O., Mudgett, M.B.,**
992 **Börnke, F., Hofius, D., and Üstün, S.** (2022). A bacterial effector counteracts host
993 autophagy by promoting degradation of an autophagy component. EMBO J **41,**
994 e110352.

Li, J., Yuan, J., Li, Y., Sun, H., Ma, T., Huai, J., Yang, W., Zhang, W., and Lin, R. (2022). The CDC48 complex mediates ubiquitin-dependent degradation of intra-chloroplast proteins in plants. Cell Rep **39,** 110664.

Ling, Q., Huang, W., Baldwin, A., and Jarvis, P. (2012). Chloroplast biogenesis is regulated by direct action of the ubiquitin-proteasome system. Science **338,** 655-659.

Ling, Q., Broad, W., Trösch, R., Töpel, M., Demiral Sert, T., Lymperopoulos, P., Baldwin, A., and Jarvis, R.P. (2019). Ubiquitin-dependent chloroplast-associated protein degradation in plants. Science **363,** eaav4467.

Lung, S.C., Smith, M.D., and Chuong, S.D. (2015). Isolation of Chloroplasts from Plant Protoplasts. Cold Spring Harb Protoc **2015,** 895-899.

McLoughlin, F., Augustine, R.C., Marshall, R.S., Li, F., Kirkpatrick, L.D., Otegui, M.S., and Vierstra, R.D. (2018). Maize multi-omics reveal roles for autophagic recycling in proteome remodelling and lipid turnover. Nat Plants **4,** 1056-1070.

Michaeli, S., Honig, A., Levanony, H., Peled-Zehavi, H., and Galili, G. (2014). Arabidopsis ATG8-INTERACTING PROTEIN1 is involved in autophagy-dependent vesicular trafficking of plastid proteins to the vacuole. Plant Cell **26,** 4084-4101.

Mizushima, N., Noda, T., Yoshimori, T., Tanaka, Y., Ishii, T., George, M.D., Klionsky, D.J., Ohsumi, M., and Ohsumi, Y. (1998). A protein conjugation system essential for autophagy. Nature **395,** 395-398.

Nakamura, S., Hidema, J., Sakamoto, W., Ishida, H., and Izumi, M. (2018). Selective elimination of membrane-damaged chloroplasts via microautophagy. Plant Physiol **177,** 1007-1026.

Nezis, I.P., Simonsen, A., Sagona, A.P., Finley, K., Gaumer, S., Contamine, D., Rusten, T.E., Stenmark, H., and Brech, A. (2008). Ref(2)P, the Drosophila melanogaster homologue of mammalian p62, is required for the formation of protein aggregates in adult brain. J Cell Biol **180,** 1065-1071.

Nishimura, K., Kato, Y., and Sakamoto, W. (2017). Essentials of proteolytic machineries in chloroplasts. Mol Plant **10,** 4-19.

Noda, N.N., Kumeta, H., Nakatogawa, H., Satoo, K., Adachi, W., Ishii, J., Fujioka, Y., Ohsumi, Y., and Inagaki, F. (2008). Structural basis of target recognition by Atg8/LC3 during selective autophagy. Genes Cells **13,** 1211-1218.

Ohsumi, Y. (2001). Molecular dissection of autophagy: two ubiquitin-like systems. Nat Rev Mol Cell Biol. **2,** 211-216.

Oikawa, K., Goto-Yamada, S., Hayashi, Y., Takahashi, D., Kimori, Y., Shibata, M., Yoshimoto, K., Takemiya, A., Kondo, M., Hikino, K., Kato, A., Shimoda, K., Ueda, H., Uemura, M., Numata, K., Ohsumi, Y., Hara-Nishimura, I., Mano, S., Yamada, K., and Nishimura, M. (2022). Pexophagy suppresses ROS-induced damage in leaf cells under high-intensity light. Nat Commun **13,** 7493.

Otegui, M.S. (2018). Vacuolar degradation of chloroplast components: autophagy and beyond. J Exp Bot **69,** 741-750.

Perez-Riverol, Y., Zorin, A., Dass, G., Vu, M.T., Xu, P., Glont, M., Vizcaíno, J.A., Jarnuczak, A.F., Petryszak, R., Ping, P., and Hermjakob, H. (2019). Quantifying the impact of public omics data. Nat Commun **10,** 3512.

Rasmussen, N.L., Kournoutis, A., Lamark, T., and Johansen, T. (2022). NBR1: The archetypal selective autophagy receptor. J Cell Biol **221,** e202208092.

Rowland, E., Kim, J., Friso, G., Poliakov, A., Ponnala, L., Sun, Q., and van Wijk, K.J. (2022). The CLP and PREP protease systems coordinate maturation and degradation of the chloroplast proteome in Arabidopsis thaliana. New Phytol **236,** 1339-1357.

Scheuring, D., Schöller, M., Kleine-Vehn, J., and Löfke, C. (2015). Vacuolar staining methods in plant cells. Methods Mol Biol **1242,** 83-92.

Schindelin, J., Arganda-Carreras, I., Frise, E., Kaynig, V., Longair, M., Pietzsch, T., Preibisch, S., Rueden, C., Saalfeld, S., Schmid, B., Tinevez, J.Y., White, D.J., Hartenstein, V., Eliceiri, K., Tomancak, P., and Cardona, A. (2012). Fiji: an open-source platform for biological-image analysis. Nat Methods **9,** 676-682.

Seibenhener, M.L., Babu, J.R., Geetha, T., Wong, H.C., Krishna, N.R., and Wooten, M.W. (2004). Sequestosome 1/p62 is a polyubiquitin chain binding protein involved in ubiquitin proteasome degradation. Mol Cell Biol **24,** 8055-8068.

Silva, J.C., Gorenstein, M.V., Li, G.Z., Vissers, J.P., and Geromanos, S.J. (2006). Absolute quantification of proteins by LCMSE: a virtue of parallel MS acquisition. Mol Cell Proteomics **5,** 144-156.

Song, Y., Feng, L., Alyafei, M.A.M., Jaleel, A., and Ren, M. (2021). Function of chloroplasts in plant stress responses. Int J Mol Sci **22,** 13464.

Spitzer, C., Li, F., Buono, R., Roschzttardtz, H., Chung, T., Zhang, M., Osteryoung, K.W., Vierstra, R.D., and Otegui, M.S. (2015). The endosomal protein CHARGED MULTIVESICULAR BODY PROTEIN1 regulates the autophagic turnover of plastids in Arabidopsis. Plant Cell **27,** 391-402.

Stringer, C., Wang, T., Michaelos, M., and Pachitariu, M. (2021). Cellpose: a generalist algorithm for cellular segmentation. Nat Methods **18,** 100-106.

Sun, S., Feng, L., Chung, K.P., Lee, K.M., Cheung, H.H., Luo, M., Ren, K., Law, K.C., Jiang, L., Wong, K.B., and Zhuang, X. (2022a). Mechanistic insights into an atypical interaction between ATG8 and SH3P2 in Arabidopsis thaliana. Autophagy **18,** 1350-1366.

Sun, Y., Yao, Z., Ye, Y., Fang, J., Chen, H., Lyu, Y., Broad, W., Fournier, M., Chen, G., Hu, Y., Mohammed, S., Ling, Q., and Jarvis, R.P. (2022b). Ubiquitin-based pathway acts inside chloroplasts to regulate photosynthesis. Sci Adv **8,** eabq7352.

Svenning, S., Lamark, T., Krause, K., and Johansen, T. (2011). Plant NBR1 is a selective autophagy substrate and a functional hybrid of the mammalian autophagic adapters NBR1 and p62/SQSTM1. Autophagy **7,** 993-1010.

Thirumalaikumar, V.P., Gorka, M., Schulz, K., Masclaux-Daubresse, C., Sampathkumar, A., Skirycz, A., Vierstra, R.D., and Balazadeh, S. (2021). Selective autophagy regulates heat stress memory in Arabidopsis by NBR1-mediated targeting of HSP90.1 and ROF1. Autophagy **17,** 2184-2199.

Turco, E., Savova, A., Gere, F., Ferrari, L., Romanov, J., Schuschnig, M., and Martens, S. (2021). Reconstitution defines the roles of p62, NBR1 and TAX1BP1 in ubiquitin condensate formation and autophagy initiation. Nat Commun **12,** 5212.

Tyanova, S., Temu, T., Sinitcyn, P., Carlson, A., Hein, M.Y., Geiger, T., Mann, M., and Cox, J. (2016). The Perseus computational platform for comprehensive analysis of (prote)omics data. Nat Methods **13,** 731-740.

Üstün, S., Hafrén, A., Liu, Q., Marshall, R.S., Minina, E.A., Bozhkov, P.V., Vierstra, R.D., and Hofius, D. (2018). Bacteria exploit autophagy for proteasome degradation and enhanced virulence in plants. Plant Cell **30,** 668-685.

Wang, J., Zhang, Q., Bao, Y., and Bassham, D. (2022). Autophagic degradation of membrane-bound organelles in plants. Biosci Rep **in press**.

Wang, Y., Yu, B., Zhao, J., Guo, J., Li, Y., Han, S., Huang, L., Du, Y., Hong, Y., Tang, D., and Liu, Y. (2013). Autophagy contributes to leaf starch degradation. Plant Cell **25,** 1383-1399.

Wang, Y.Y., Zhang, J., Liu, X.M., Li, Y., Sui, J., Dong, M.Q., Ye, K., and Du, L.L. (2021). Molecular and structural mechanisms of ZZ domain-mediated cargo selection by Nbr1. EMBO J **40,** e107497.

Wijerathna-Yapa, A., Signorelli, S., Fenske, R., Ganguly, D.R., Stroeher, E., Li, L., Pogson, B.J., Duncan, O., and Millar, A.H. (2021). Autophagy mutants show delayed chloroplast development during de-etiolation in carbon limiting conditions. Plant J **108,** 459-477.

Woodson, J.D., Joens, M.S., Sinson, A.B., Gilkerson, J., Salome, P.A., Weigel, D., Fitzpatrick, J.A., and Chory, J. (2015). Ubiquitin facilitates a quality-control pathway that removes damaged chloroplasts. Science **350,** 450-454.

Xie, Z., Nair, U., and Klionsky, D.J. (2008). Atg8 controls phagophore expansion during autophagosome formation. Mol Biol Cell **19,** 3290-3298.

Yoo, S.D., Cho, Y.H., and Sheen, J. (2007). Arabidopsis mesophyll protoplasts: a versatile cell system for transient gene expression analysis. Nat Protoc **2,** 1565-1572.

Young, P.G., Passalacqua, M.J., Chappell, K., Llinas, R.J., and Bartel, B. (2019). A facile forward-genetic screen for Arabidopsis autophagy mutants reveals twenty-one loss-of-function mutations disrupting six ATG genes. Autophagy **15,** 941-959.

Zhang, Y., and Chen, Z. (2020). Broad and complex roles of NBR1-mediated selective autophagy in plant stress responses. Cells **9,** 2562.

Zhou, J., Wang, J., Cheng, Y., Chi, Y.J., Fan, B., Yu, J.Q., and Chen, Z. (2013). NBR1-mediated selective autophagy targets insoluble ubiquitinated protein aggregates in plant stress responses. PLoS Genet **9,** e1003196.

Zhou, J., Zhang, Y., Qi, J., Chi, Y., Fan, B., Yu, J.Q., and Chen, Z. (2014). E3 ubiquitin ligase CHIP and NBR1-mediated selective autophagy protect additively against proteotoxicity in plant stress responses. PLoS Genet **10,** e1004116.

Zientara-Rytter, K., and Sirko, A. (2014). Significant role of PB1 and UBA domains in multimerization of Joka2, a selective autophagy cargo receptor from tobacco. Front Plant Sci **5,** 13.

Zientara-Rytter, K., Lukomska, J., Moniuszko, G., Gwozdecki, R., Surowiecki, P., Lewandowska, M., Liszewska, F., Wawrzyńska, A., and Sirko, A. (2011). Identification and functional analysis of Joka2, a tobacco member of the family of selective autophagy cargo receptors. Autophagy **7,** 1145-1158.

Supplemental Tables

Supplemental Table 1: Proteins identified by at least 2 peptide spectral matches.

Supplemental Table 2: Normalized protein abundances based on the average of two technical replicates or used directly if the proteins were only detected in one technical replicate.

Supplemental Table 3: Protein abundances expressed as Log2 values.

Supplemental Table 4: Relative changes of protein abundance between LL and HL conditions in WT plants. Analysis was performed using the Perseus platform 2.0.6.0 (Tyanova et al., 2016), intensity values from mass spectrometry were log2 imputed and missing values were replaced with random numbers from a Gaussian distribution with a width of 0.3 and a downshift of 1.8. Statistical significance was determined using t-tests. The protein localizations and functions were categorized based on the GO term listed below. GO:0006914 (Autophagy), GO:0000502 (Proteasome), GO:0009507 (Chloroplast), GO:0005739 (Mitochondria), GO:0005777 (Peroxisome), GO:0005840 (Ribosome), GO:0009941 (Chloroplast envelope), GO:0009570 (Chloroplast stroma) and GO:0009534 (Chloroplast thylakoid).

Supplemental Table 5: Relative changes of protein abundance between LL and HL conditions in the *atg7* mutant. Analysis was performed using the Perseus platform 2.0.6.0 (Tyanova et al., 2016), intensity values from mass spectrometry were log2 imputed and missing values were replaced with random numbers from a Gaussian distribution with a width of 0.3 and a downshift of 1.8. Statistical significance was determined using t-tests. The protein localizations and functions were categorized based on the GO term listed below. GO:0006914 (Autophagy), GO:0000502 (Proteasome), GO:0009507 (Chloroplast), GO:0005739 (Mitochondria), GO:0005777 (Peroxisome), GO:0005840 (Ribosome), GO:0009941 (Chloroplast envelope), GO:0009570 (Chloroplast stroma) and GO:0009534 (Chloroplast thylakoid).

Supplemental Table 6: Relative changes of protein abundance between LL and HL conditions in the *nbr1* mutant. Analysis was performed using the Perseus platform 2.0.6.0 (Tyanova et al., 2016), intensity values from mass spectrometry were log2 imputed and missing values were replaced with random numbers from a Gaussian distribution with a width of 0.3 and a downshift of 1.8. Statistical significance was determined using t-tests. The protein localizations and functions were categorized based on the GO term listed below. GO:0006914 (Autophagy), GO:0000502 (Proteasome), GO:0009507 (Chloroplast), GO:0005739 (Mitochondria), GO:0005777 (Peroxisome), GO:0005840 (Ribosome), GO:0009941 (Chloroplast envelope), GO:0009570 (Chloroplast stroma) and GO:0009534 (Chloroplast thylakoid).

Supplemental Table 7: Relative changes of protein abundance between LL and HL conditions in the *nbr1 atg7* double mutant. Analysis was performed using the Perseus platform 2.0.6.0 (Tyanova et al., 2016), intensity values from mass spectrometry were log2 imputed and missing values were replaced with random numbers from a Gaussian distribution with a width of 0.3 and a downshift of 1.8. Statistical significance was determined using t-tests. The protein localizations and functions were categorized based on the GO term listed below. GO:0006914 (Autophagy), GO:0000502 (Proteasome), GO:0009507 (Chloroplast), GO:0005739 (Mitochondria), GO:0005777 (Peroxisome), GO:0005840 (Ribosome), GO:0009941 (Chloroplast envelope), GO:0009570 (Chloroplast stroma) and GO:0009534 (Chloroplast thylakoid).

Supplemental Table 8: Comparison of protein abundances between WT and the *atg7* mutant under HL conditions. Analysis was performed using the Perseus platform 2.0.6.0 (Tyanova et al., 2016), intensity values from mass spectrometry were log2 imputed and missing values were replaced with random numbers from a Gaussian distribution with a width of 0.3 and a downshift of 1.8. Statistical significance was determined using t-tests. The protein localizations and functions were categorized based on the GO term listed below. GO:0006914 (Autophagy), GO:0000502 (Proteasome), GO:0009507 (Chloroplast), GO:0005739 (Mitochondria), GO:0005777 (Peroxisome), GO:0005840 (Ribosome), GO:0009941 (Chloroplast envelope), GO:0009570 (Chloroplast stroma) and GO:0009534 (Chloroplast thylakoid).

Supplemental Table 9: Comparison of protein abundances between WT and the *nbr1* mutant under HL conditions. Analysis was performed using the Perseus platform 2.0.6.0 (Tyanova et al., 2016), intensity values from mass spectrometry were log2 imputed and missing values were replaced with random numbers from a Gaussian distribution with a width of 0.3 and a downshift of 1.8. Statistical significance was determined using t-tests. The protein localizations and functions were categorized based on the GO term listed below. GO:0006914 (Autophagy), GO:0000502 (Proteasome), GO:0009507 (Chloroplast), GO:0005739 (Mitochondria), GO:0005777 (Peroxisome), GO:0005840 (Ribosome), GO:0009941 (Chloroplast envelope), GO:0009570 (Chloroplast stroma) and GO:0009534 (Chloroplast thylakoid).

Supplemental Table 10: Comparison of protein abundances between WT and the *nbr1 atg7* double mutant under HL conditions. Analysis was performed using the Perseus platform 2.0.6.0 (Tyanova et al., 2016), intensity values from mass spectrometry were log2 imputed and missing values were replaced with random numbers from a Gaussian distribution with a width of 0.3 and a downshift of 1.8. Statistical significance was determined using t-tests. The protein localizations and functions were categorized based on the GO term listed below. GO:0006914 (Autophagy),

GO:0000502 (Proteasome), GO:0009507 (Chloroplast), GO:0005739 (Mitochondria), GO:0005777 (Peroxisome), GO:0005840 (Ribosome), GO:0009941 (Chloroplast envelope), GO:0009570 (Chloroplast stroma) and GO:0009534 (Chloroplast thylakoid).

Supplemental Table 11: Comparison of protein abundances between WT and the *atg7* mutant under LL conditions. Analysis was performed using the Perseus platform 2.0.6.0 (Tyanova et al., 2016), intensity values from mass spectrometry were log2 imputed and missing values were replaced with random numbers from a Gaussian distribution with a width of 0.3 and a downshift of 1.8. Statistical significance was determined using t-tests. The protein localizations and functions were categorized based on the GO term listed below. GO:0006914 (Autophagy), GO:0000502 (Proteasome), GO:0009507 (Chloroplast), GO:0005739 (Mitochondria), GO:0005777 (Peroxisome), GO:0005840 (Ribosome), GO:0009941 (Chloroplast envelope), GO:0009570 (Chloroplast stroma) and GO:0009534 (Chloroplast thylakoid).

Supplemental Table 12: Comparison of protein abundances between WT and the *nbr1* mutant under LL conditions. Analysis was performed using the Perseus platform 2.0.6.0 (Tyanova et al., 2016), intensity values from mass spectrometry were log2 imputed and missing values were replaced with random numbers from a Gaussian distribution with a width of 0.3 and a downshift of 1.8. Statistical significance was determined using t-tests. The protein localizations and functions were categorized based on the GO term listed below. GO:0006914 (Autophagy), GO:0000502 (Proteasome), GO:0009507 (Chloroplast), GO:0005739 (Mitochondria), GO:0005777 (Peroxisome), GO:0005840 (Ribosome), GO:0009941 (Chloroplast envelope), GO:0009570 (Chloroplast stroma) and GO:0009534 (Chloroplast thylakoid).

Supplemental Table 13: Comparison of protein abundances between WT and the *nbr1 atg7* double mutant under LL conditions. Analysis was performed using the Perseus platform 2.0.6.0 (Tyanova et al., 2016), intensity values from mass spectrometry were log2 imputed and missing values were replaced with random numbers from a Gaussian distribution with a width of 0.3 and a downshift of 1.8. Statistical significance was determined using t-tests. The protein localizations and functions were categorized based on the GO term listed below. GO:0006914 (Autophagy), GO:0000502 (Proteasome), GO:0009507 (Chloroplast), GO:0005739 (Mitochondria), GO:0005777 (Peroxisome), GO:0005840 (Ribosome), GO:0009941 (Chloroplast envelope), GO:0009570 (Chloroplast stroma) and GO:0009534 (Chloroplast thylakoid).

Supplemental Table 14: Primers used for genotyping.

Supplemental Data: Data used for all graphs presented in this study.

Figure 2G source data: Original files of full raw unedited blots and figure with uncropped blots.

1222 **Figure 2-figure supplement 1:** Original files of full raw unedited blots. Uncropped blots are
1223 shown in Fig.2-figure supplement 1.

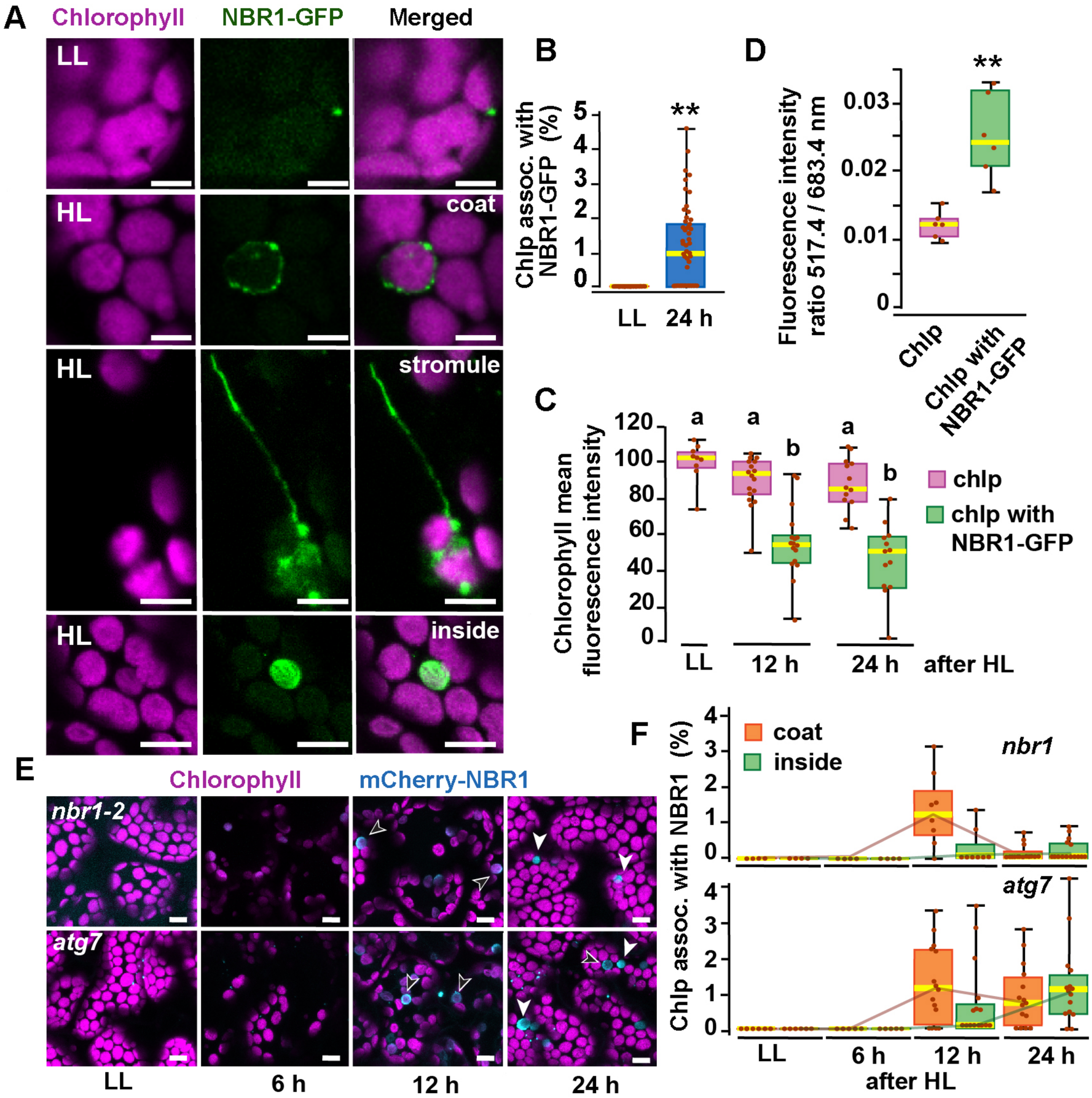

Figure 1

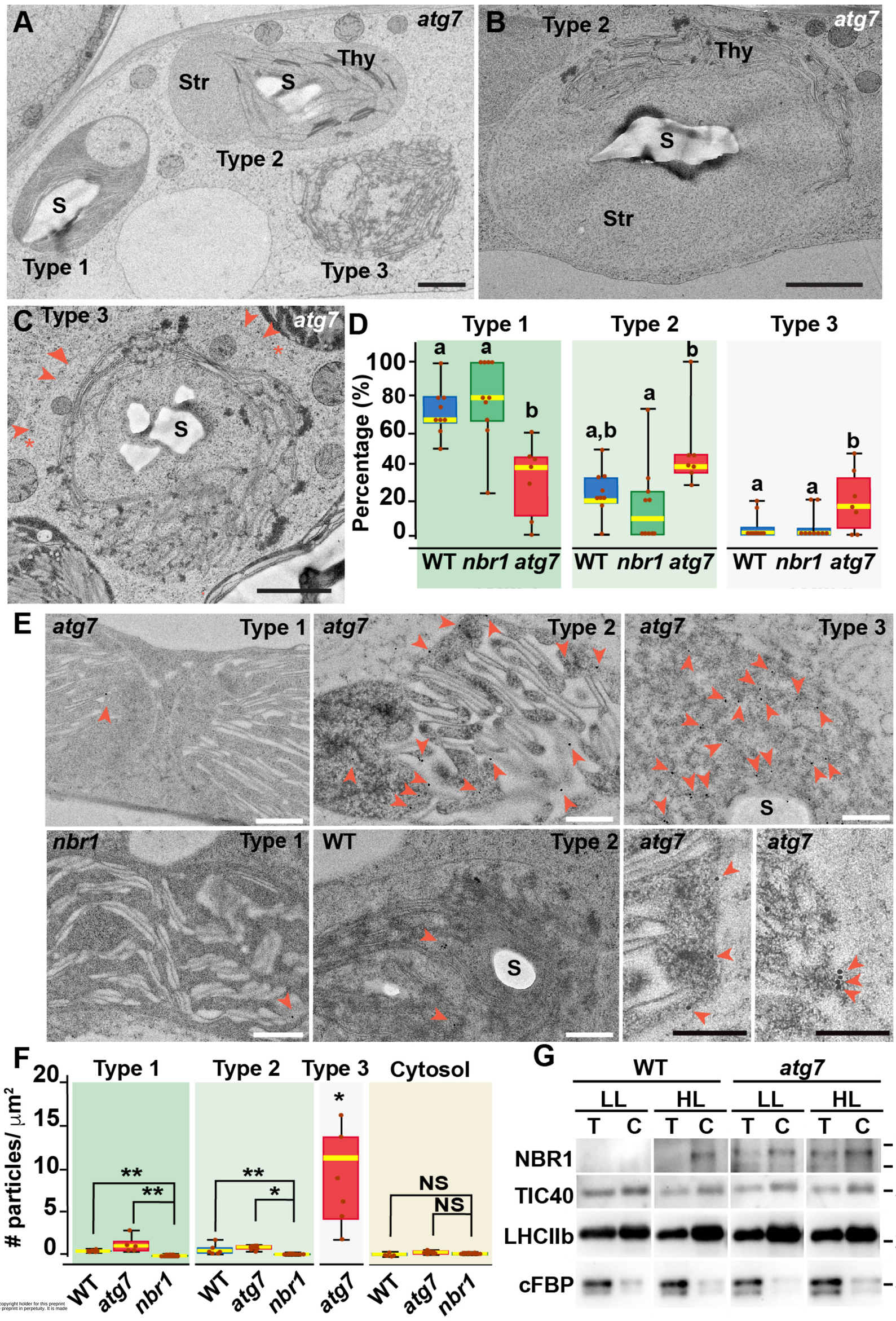

Figure 2

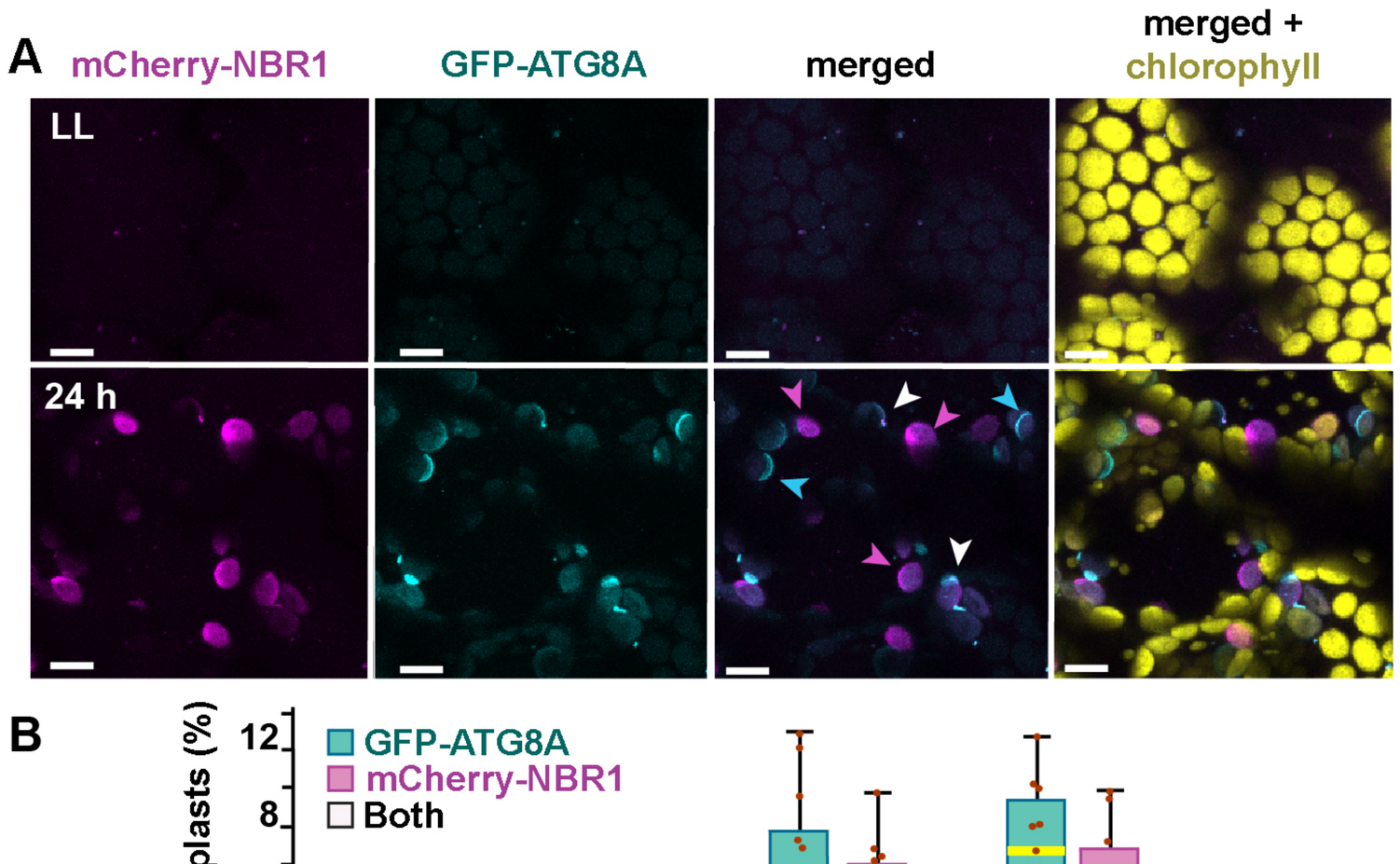

Figure 3

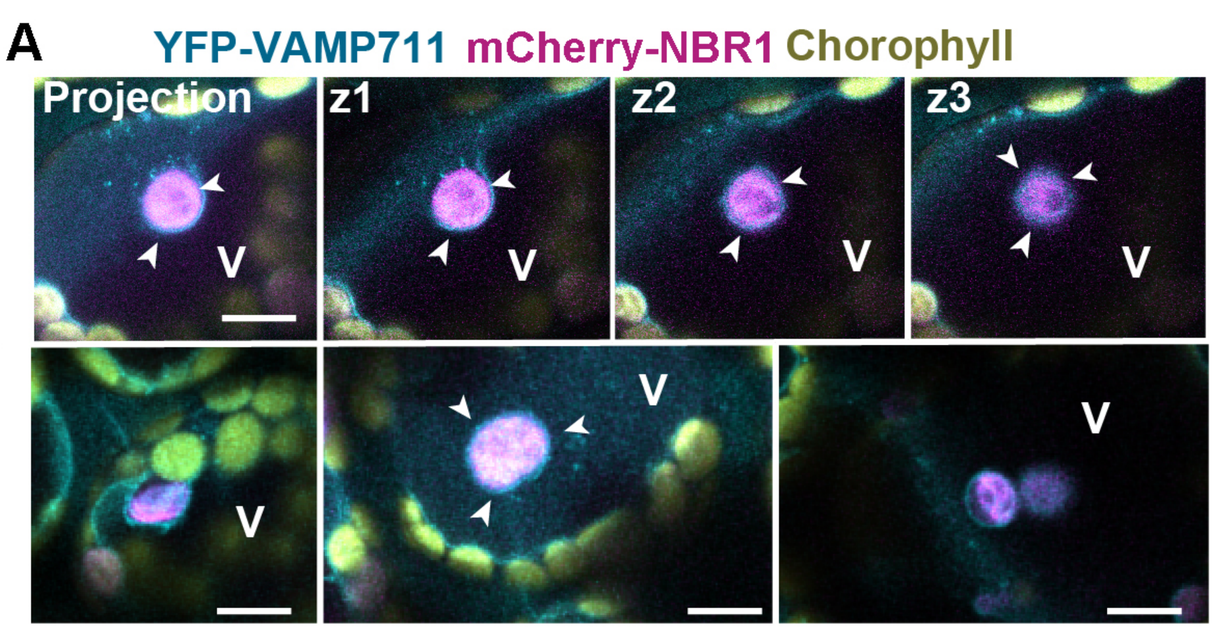

Figure 4

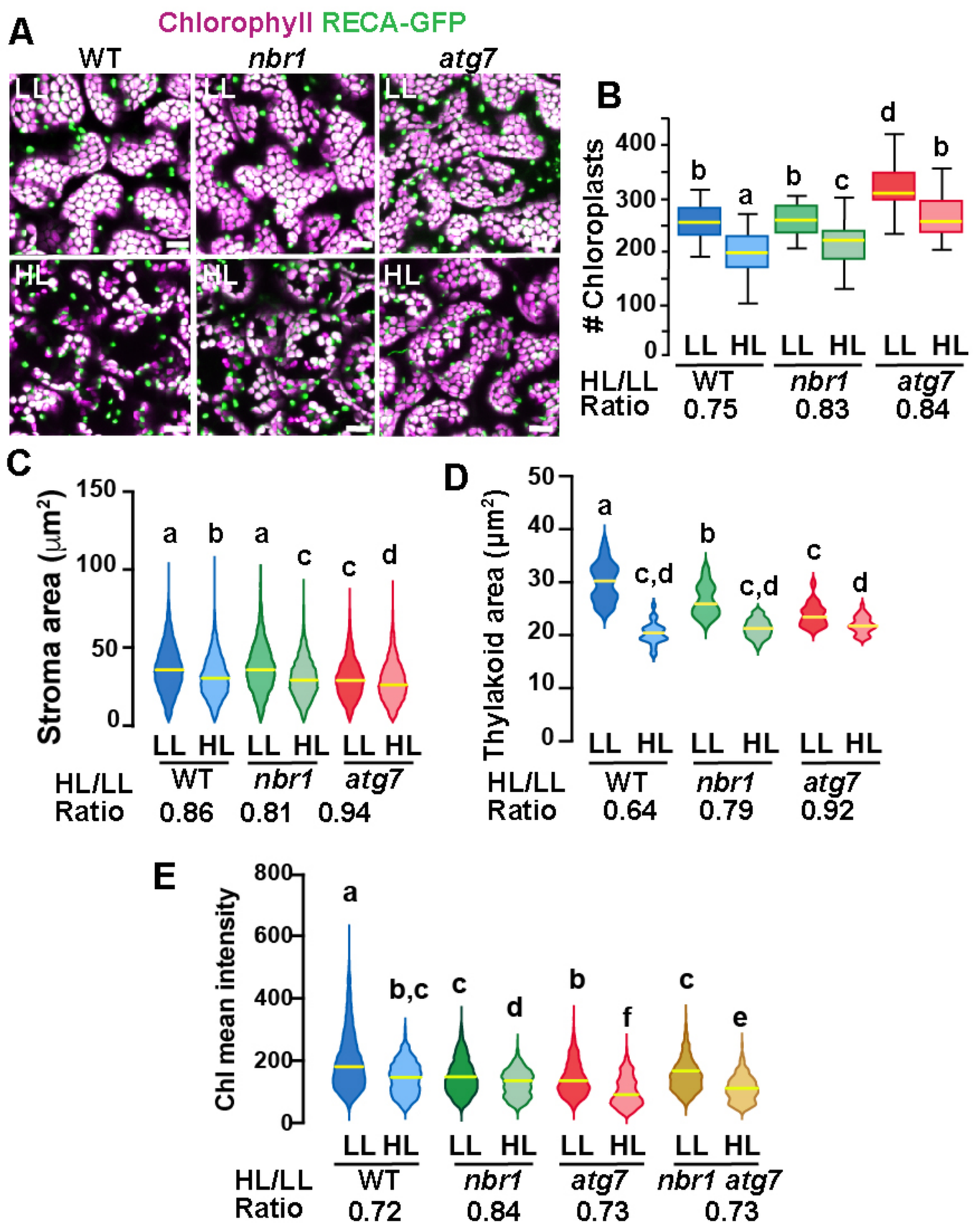

Figure 5

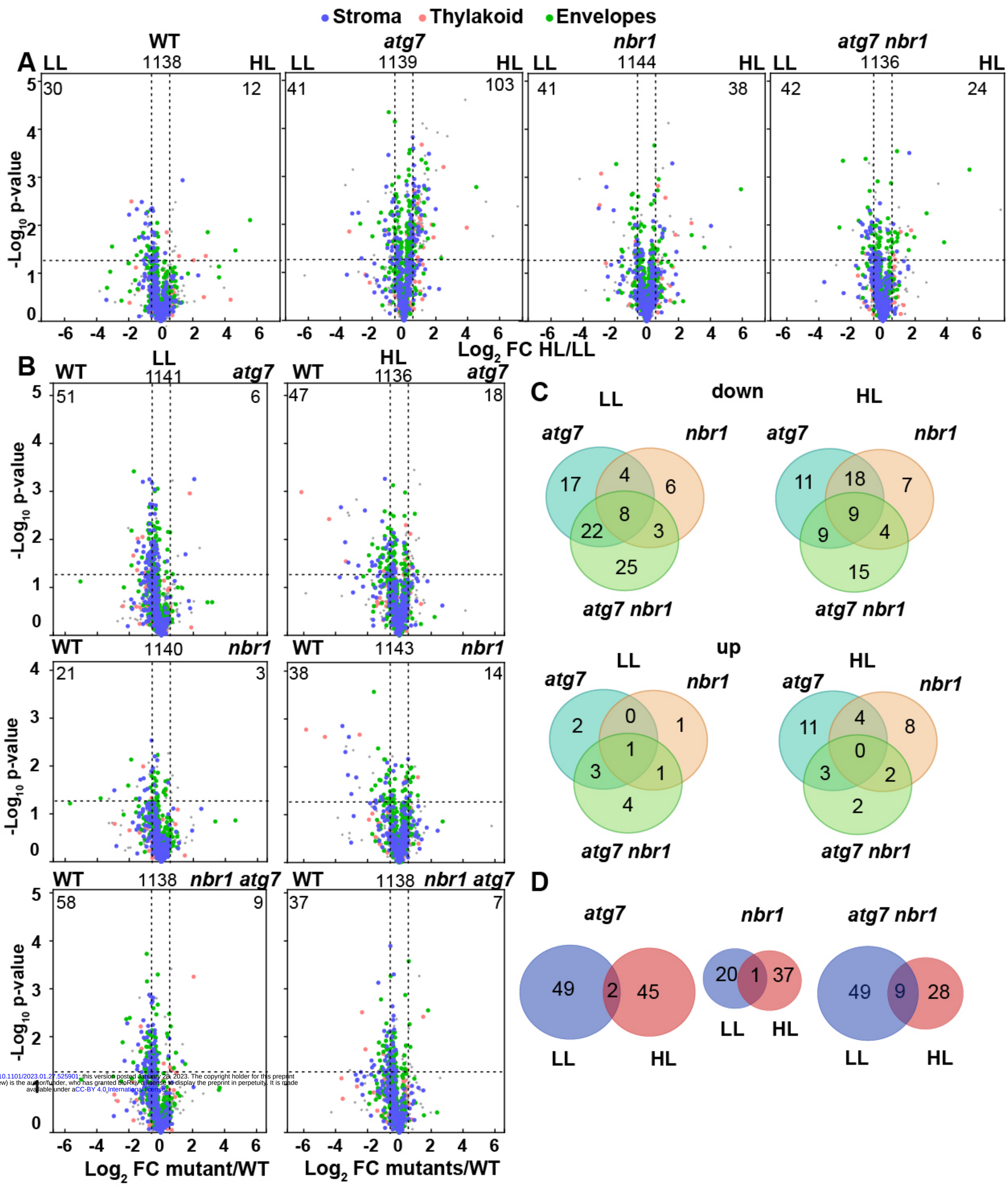

Figure 6

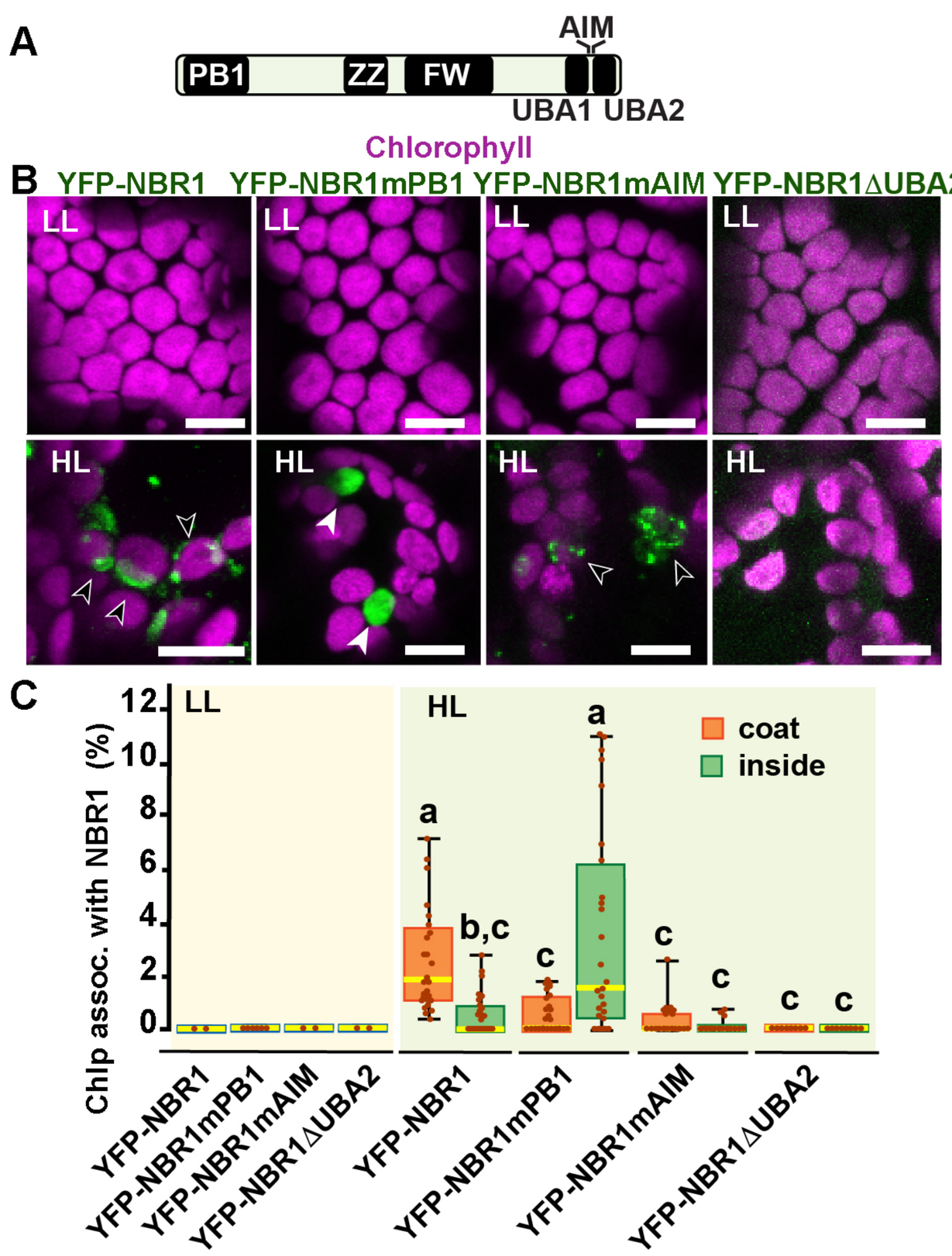

Figure 7

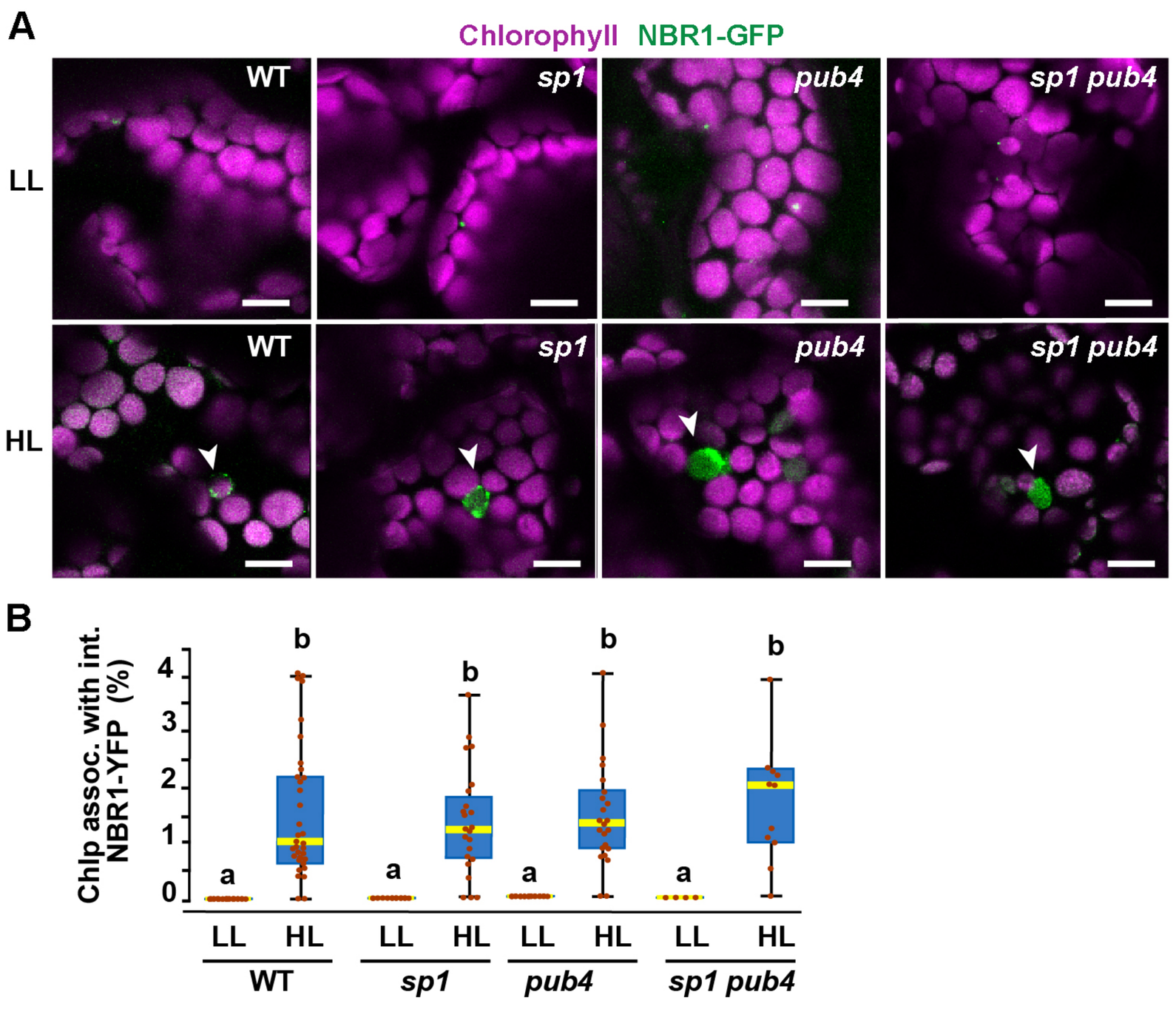

Figure 8

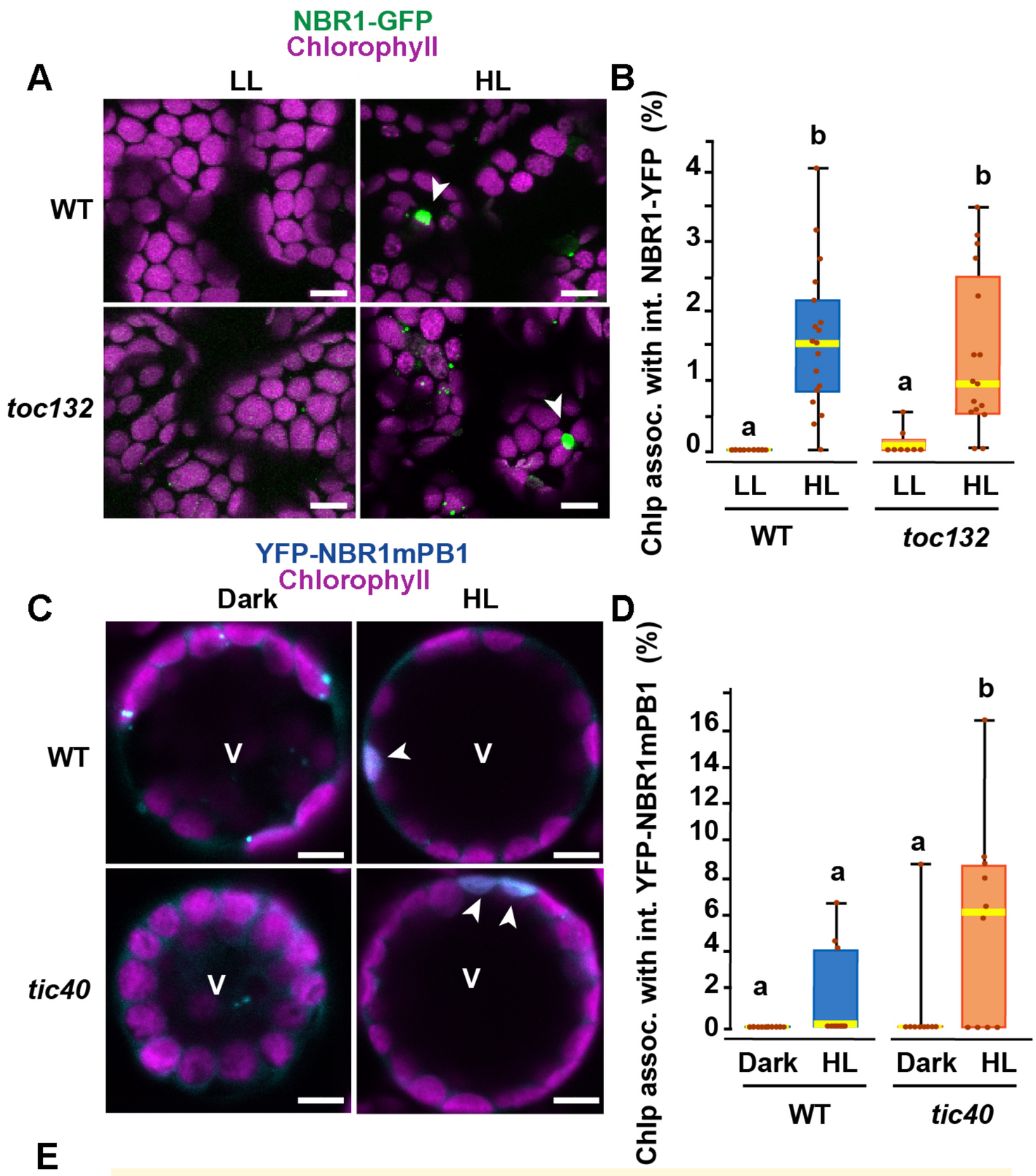

Figure 9

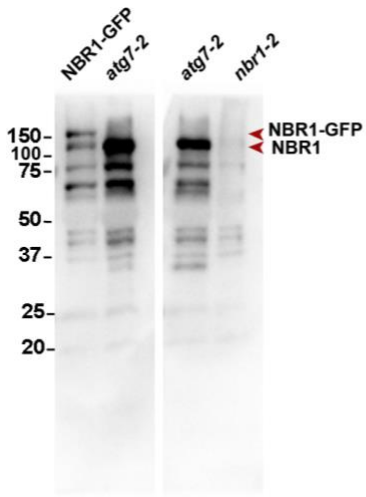

Figure 2-figure supplement 1: Uncropped immunoblot of total proteins from wild type plants expressing NBR1-GFP, and *atg7-1* and *nbr1* mutants using anti-NBR1 antibodies (Jung et al., 2020).

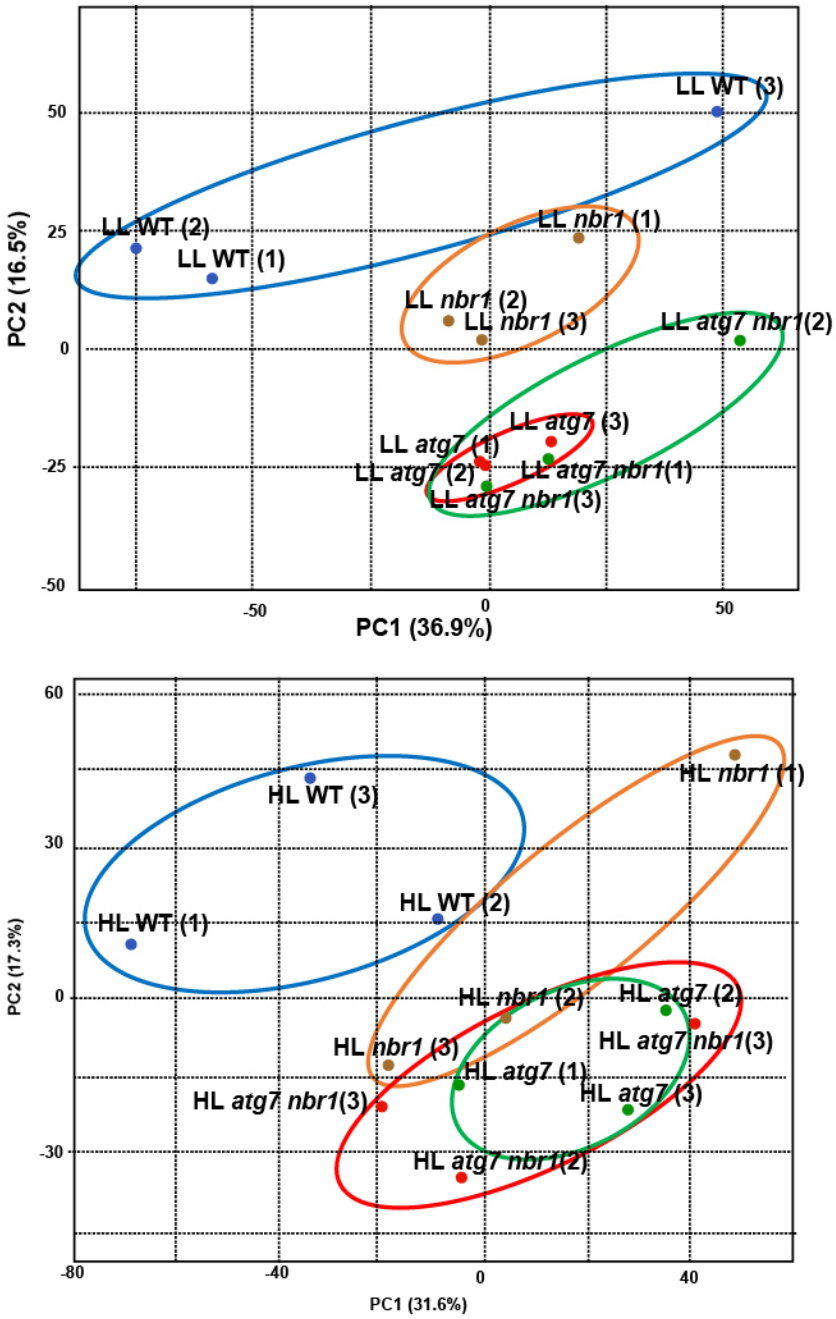

Figure 6-figure supplement 1: Principal component analysis (PCA) of proteomic analysis samples. The plot depicts each biological replicate used for the proteomic analysis from WT Col-0, *atg7*, *nbr1* and *nbr1 atg7* plants either under LL or after HL exposure.

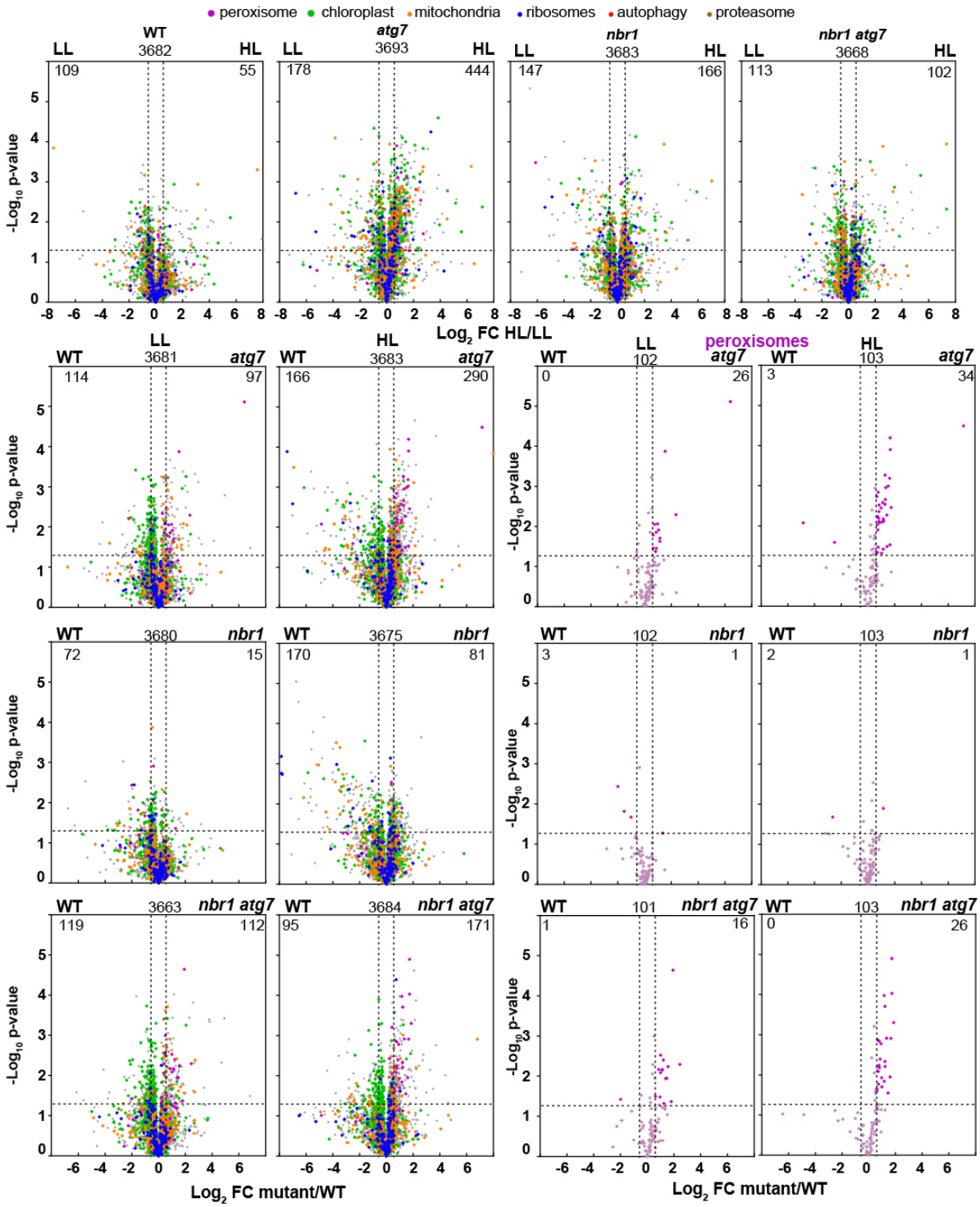

Figure 6-figure supplement 2: Proteome analysis by liquid chromatography-tandem mass spectrometry (LC-MS/MS).

(A) Volcano plots showing the relative abundance changes of total selected protein in wild type (Col-0), *nbr1*, *atg7*, and *nbr1 atg7* seedlings grown either under LL or exposed to HL and let

recover for 24 h. Proteins were identified by LC-MS/MS, and their average abundances were calculated from the MS1 precursor ion intensities. Only proteins with at least two peptide spectral matches were considered in the analysis. Each protein is plotted based on its Log_2 FC in abundance (HL/LL) and its $-log_{10}$ *p*-value in significance based on the three biological replicates.

(B) Volcano plots showing the relative abundance changes of total selected protein in mutants compared to wild type (Col-0) either under different light conditions.

(C) Volcano plots showing the relative abundance changes of peroxisomal protein in mutants compared to wild type (Col-0) either under different light conditions.

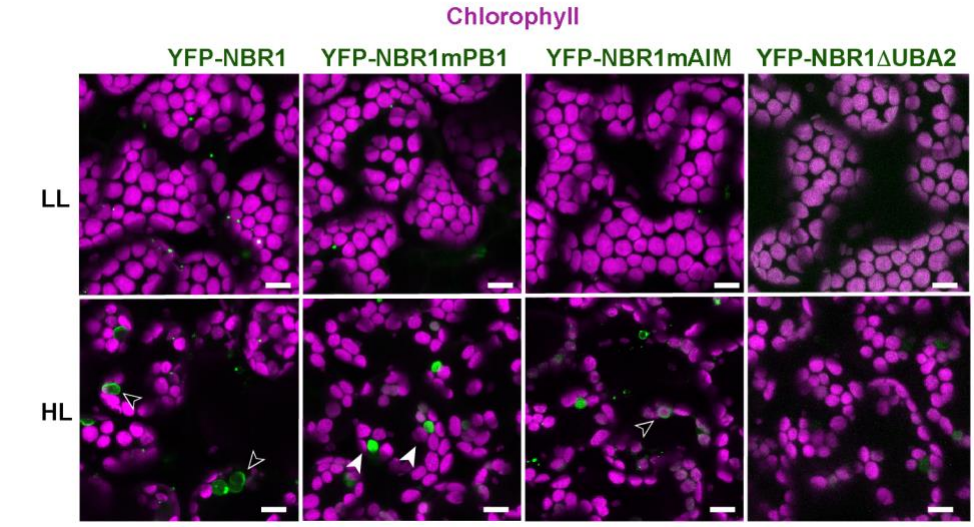

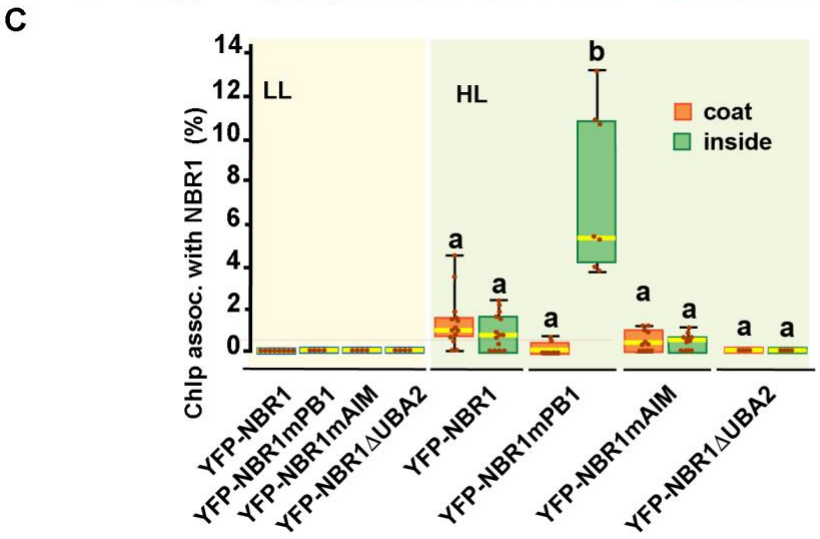

Figure 7-figure supplement 1: NBR1 domains in NBR1 recruitment to chloroplasts in *nbr1 atg7* double mutant cotyledons after HL treatment.

(A) Confocal imaging of NBR1 mutated proteins fused to YFP expressed in 8-day old *nbr1 atg7* seedlings grown under LL (top) or 24 h after HL exposure (bottom). Hollow arrowheads and filled arrowheads indicate YFP-NBR1 coating chloroplasts and inside chloroplasts, respectively.

(C) Box and whisker plots show the percentage of chloroplast associated with the YFP-labeled mutated NBR1 proteins, localized to either coats (orange) or inside chloroplasts (green). Boxes show the variation in data through quartiles; the middle line indicates the median and whiskers show the upper and lower fences.

Scale bars: 10 μm in A.